This Book of Proceedings contains the extended abstracts of the contributions presented at the DIPSI Workshop 2023 on Droplet Impact Phenomena and Spray Investigation, organised by the University of Bergamo on Friday 16th June 2023 in Bergamo, Italy.

This workshop, which is now at its fifteenth edition, represents an important opportunity to share the recent knowledge on droplets and sprays in a variety of research fields and industrial applications.

The event is supported by the Department of Engineering and Applied Sciences of the University of Bergamo and the Research Training Group 2160/2 DROPIT in collaboration with the University of Stuttgart.


GIANPIETRO ELVIO COSSALI is full professor of Thermal Physics at the Department of Engineering and Applied Sciences of the University of Bergamo. His research activity is carried out in the field of thermo-fluid dynamics of multiphase systems, with particular reference to the characterization of sprays, to the dynamics of the interaction between droplets and solid and liquid surfaces and to the analytical modelling of heat and mass exchange in dispersed flows. He teaches the course of Thermal Physics, Thermo-fluid-dynamics and Heat transfer at the University of Bergamo.

SIMONA TONINI is is Associate Professor of Thermal Physics at the Department of Engineering and Applied Sciences of the University of Bergamo. His research is carried out in the field of theoretical and numerical modeling of transport phenomena in multiphase flows. She teaches the course of Thermal Physics and HVAC Systems and the course of Thermal Physics for Advanced Technology for the Engineering degrees at the University of Bergamo.



ISBN: 978-88-97413-82-0
DOI: 10.13122/DIPSI2023


PROCEEDINGS OF THE DIPSI WORKSHOP 2023

# PROCEEDINGS OF THE DIPSI WORKSHOP 2023

## Droplet Impact Phenomena & Spray Investigations

## BERGAMO, ITALY, 16th JUNE 2023


Edited by Gianpietro Elvio Cossali, Simona Tonini



UNIVERSITÀ DEGLI STUDI DI BERGAMO

2023

# PROCEEDINGS
# OF THE
# DIPSI WORKSHOP 2023

## Droplet Impact Phenomena
## & Spray Investigations

## BERGAMO, ITALY, 16th JUNE 2023

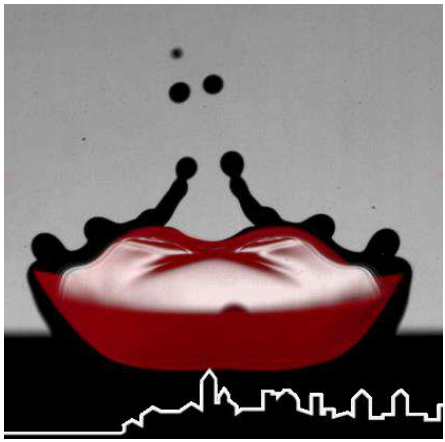

**Edited by Gianpietro Cossali, Simona Tonini**

**Università degli Studi di Bergamo**
**2023**

PROCEEDINGS OF THE DIPSI WORKSHOP 2023: Droplet Impact Phenomena & Spray investigations, Bergamo, Italy, 16th July 2023 / edited by Gianpietro Elvio Cossali – Bergamo: Università degli Studi di Bergamo, 2023.
**ISBN:** 978-88-97413-82-0
**DOI:** 10.13122/DIPSI2023



Progetto grafico:
Servizi Editoriali – Università degli Studi di Bergamo
Università degli Studi di Bergamo
via Salvecchio, 19
24129 Bergamo
Cod. Fiscale 80004350163
P. IVA 01612800167

https://aisberg.unibg.it/handle/10446/234208

# Workshop agenda, Friday 16th June 2023

08:45 Registration

09:00 Welcome speech

09:15 S1 Drop/wall interaction

9:15 R. Akbari, W. Yu, A. Bagni, R. Ruffo, M.-J. Thoraval and C. Antonini, *Understanding water drop impact on porous meshes for effective fog harvesting*

9:45 A.K. Geppert and B. Weigand, *Ground spreading dynamics during single droplet impact onto a free-standing cubic surface element*

10:15 Coffee break

10:45 S2 Drop/drop interaction

10:45 N. Janssen and U. Janoske, *Experimental and numerical investigation of particle-droplet-substrate interaction*

11:15 C. Chasos, *Spray injection and development realizations and investigations of the effect of droplets coalescence and recirculation on ensemble-averaged predicted data*

11:45 M. Marengo, *Impact of compound drops on a flat solid surface*

12:15 Lunch break

13:30 Poster session

Y. Hu, G.E. Cossali, M. Frey, J. Reutzsch, S. Tonini and B. Weigand, *Evaporation of an oscillating drop*

D. Klötzl, M. Ibach, D. Weiskopf and B. Weigand, *Relation between shear rate and structural parameter in non-Newtonian droplet oscillations via Jacobi sets and STL decomposition: a visual analysis*

H.C. Konan and C. Rohde, *An incompressible two-phase model with hyperbolic Navier-Stokes-Cahn-Hilliard Approach*

C. Marianowski, S. Fasoulas and M. Pfeiffer, *Simulating liquid-vapor interfaces using non-equilibrium particle schemes*

P. Molina Vogelsang, S. Schubert, B. Weigand and G. Lamanna, *An approach to investigate the 3D height evolution in the crown crater during early crown formation with the general defocusing* particle tracking (GDPT) method

P. Palmetshofer, T.A. Marz and B. Weigand, *360° contact angles of water droplets on micrometric ramps, pyramids and staggered cuboid surfaces at two different wettabilities*

R. Saha and B. Weigand, *Numerical simulation of droplet impact on structured surfaces*

J. Stober, M. Santini and K. Schulte, *Experimental observation of the collision of a crown with a thin wall film during early oblique droplet impact*

R. Tietz, M. Pfeiffer and S. Fasoulas, *Simulation of sub-micrometer droplet evaporation with a particle-based spherically-symmetric Enskog-Vlasov solver*

Z. Zhang and S. Vanapalli, *Dynamics of a nitrogen Leidenfrost droplet inside a water pool*

14:15 S3 Phase change

14:15 S. Jöns, P. Mossier, C.-D. Munz and A. Beck, *The use of local solutions to model phase transitions in the compressible flow regime*

14:45 V. Kunberger, *Phase change and interaction behaviour of supercooled Water droplets*

**15:15 S4 Measurement techniques**

15:15 A. Purandare, *Leidenfrost dynamics of sublimating solid carbon dioxide disc elucidated using optical coherence tomography*

**16:15 Coffee break**

**16:30 Workshop closure**


*Bergamo, 16th June 2023*

# Contents

# Ground spreading dynamics during single droplet impact onto a free-standing cubic surface element

A. K. Geppert*[1], B. Weigand[1]

[1]Institute of Aerospace Thermodynamics, University of Stuttgart, Germany
*Corresponding author: anne.geppert@itlr.uni-stuttgart.de

## Abstract

In many technical applications the impact of a single droplet onto a dry, structured surface plays an important role. Hereby, the impact dynamics are often affected also by the wettability of the respective surface. In order to gain a better understanding of the complex interplay between surface structure and wettability, the basic process of single droplet impact onto a free-standing cubic surface element with varying surface wettability is investigated experimentally. High-speed visualization of the impact process is performed with the multi-perspective experimental facility in our laboratory [1]. The experimental parameter range covers cubic pillars with varying edge length (between 1 mm and 2.4 mm) and different surface wettabilities, multiple droplet diameters, impact velocities and two fluids, namely water and isopropanol. The focus of this work is on the effects of surface wettability and drop-pillar ratio $\bar{L}_D$ on the evolution of the spreading factor $d^* = d_s/D_d$ over the duration of the impact process.

## Introduction

Single droplet impact onto dry, structured surfaces plays an important role in many technical applications. In addition to the surface structure itself, also the wettability affects the impact outcome and especially the liquids spreading behaviour. For example, the cooling of micro-electronic devices requires a high surface wettability to enhance the heat transfer, i.e. a complete as possible coverage of the surface with the cooling liquid. On the other hand, self-cleaning surfaces have a very low surface wettability to completely repel liquids. In order to

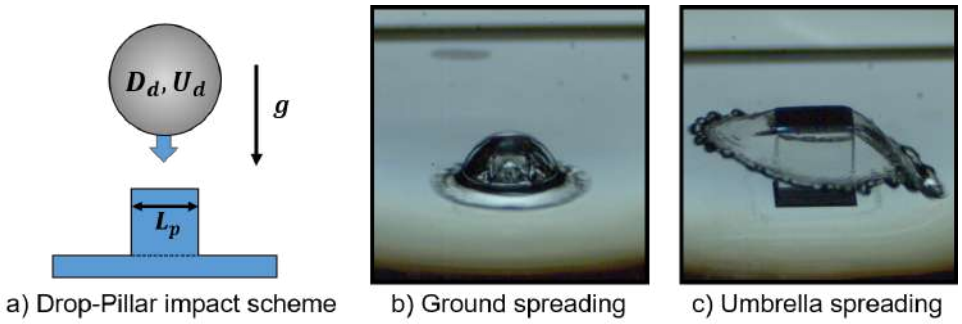


**Figure 1.** Schematic representation of droplet impact problem and observed impact morphologies.

gain a better understanding of the complex interplay between surface structure and wettability we investigated the basic process of droplet impact onto a free-standing cubic surface element (pillar) with varying surface wettability (see Fig. 1a). To begin with, the impact of an isopropanol droplet onto a pillar with 1 mm edge length, whose surface satisfied full wetting conditions, was studied with a combined numerical and experimental approach by Ren et al. [2]. It unraveled the process of air entrapment underneath the droplet and the subsequent bubble formation. Next, we expanded the parameter range to include additional pillar sizes (up to 2.4 mm) and surface wettabilities (characterized by the contact angle $\theta$), multiple droplet diameters, impact velocities and a second test liquid (water). Defining the ratio of the pillar length $L_p$ to the droplet diameter $D_d$ as characteristic non-dimensional parameter $\bar{L}_D = L_p/D_d$ (pillar-drop ratio), we

could separate two different impact morphologies. For $\bar{L}_D = L_p/D_d < 1$, *ground spreading* occurs, i.e., the droplet liquid flows around the pillar, encloses it and spreads radially on the solid target surface (see Fig. 1b). If the pillar-drop ratio is $\bar{L}_D \gtrsim 1$, *umbrella spreading* takes place. In this case, the droplet spreading starts on top of the pillar and proceeds in mid-air (see Fig. 1c). A distinctive feature of umbrella spreading is the rectangular lamella, whose corners are azimuthally rotated by 45° with respect to the pillar corners.
The present investigation focuses on the detailed analysis of the spreading dynamics of the droplet, i.e. the temporal evolution of the spreading factor $d^* = d_s/D_d$ and its maximum value $d^*_{max}$. It includes a comparison to the spreading behaviour on smooth solid surfaces.

## Experimental Facility

High-speed visualization of the impact process is performed with the multi-perspective experimental facility described in detail in Foltyn et al. [1]. The imaging systems records the droplet impact from four different perspectives (top, lateral, bottom and spatial view) and employs different imaging techniques, e.g. back-light imaging and total internal reflection method. The latter allows to clearly distinguish dry and wetted surface areas. The top, lateral and bottom views are recorded with two fully synchronized Photron SA-X2 cameras at a frame rate of 20,000 fps. The utilised optical resolutions are 17 µm/px (bottom), 18 µm/px (lateral) and 28 µm/px (top). The spatial view (see Fig. 1a,b) is recorded with a Chronos 1.4 colour camera at a frame rate of 1,000 fps and an optical resolution of 11 µm/px. The droplet is generated by regular drip off from a tilted needle. Droplet diameters of 2.0 mm and 2.4 mm and impact velocities between $1.45\ \mathrm{m\,s^{-1}}$ and $3.35\ \mathrm{m\,s^{-1}}$ are used. Before impact, the droplet passes a laser light barrier, which triggers the image acquisition. The surface specimen, i.e. the free-standing pillars with edge length between 1 mm and 2.4 mm, are made of acrylic glass. The specimens wetting behaviour was manipulated with low pressure plasma activation (full wetting conditions, $\theta \approx 0°$) and plasma polymerization (reduced wettability, $\theta \approx 71°$; low wettability $\theta \approx 120°$). Detailed information on the experimental facility and the post-processing procedures can be found in [1].

## Results and Discussion

The investigated parameter space encompasses in total 65 experiments. Note that, in case of ground spreading $d^*$ is derived from the bottom view images, while in case of umbrella spreading the top view images are used. The results focus on the effects of surface wettability and

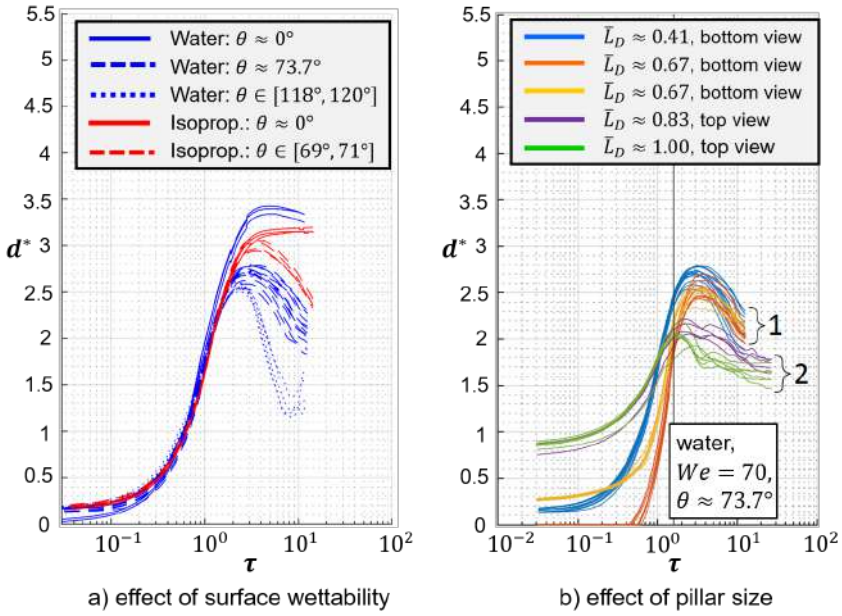


**Figure 2.** Temporal evolution of the spreading factor $d^* = d_s/D_d$.

drop-pillar ratio $\bar{L}_D$ on the temporal evolution of the spreading factor $d^* = d_s/D_d$. In Figure 2a, the effect of surface wettability is shown for the smallest pillar size ($\bar{L}_D = 0.4 - 0.5$) and the lowest impact velocity, hence only ground spreading is observed. For a fully wettable surface (solid lines), the plateau phase follows directly after the kinematic and spreading phase defined by Rioboo et al. [3]. For the water droplet (blue) a slight receding of the liquid is observable, which is not the case for isopropanol. This results from the three times higher surface tension of water compared to isopropanol. With decreasing surface wettability (dashed lines), the droplet starts to recede immediately after reaching its maximum spreading diameter. In case of water droplet impact, $d^*_{max}$ decreases strongly with decreasing surface wettability. A further decrease of surface wettability to hydrophobic conditions (dotted line) leads to an even faster droplet receeding.
The effect of the drop-pillar ratio $\bar{L}_D$ on the evolution of the spreading factor is shown in Figure 2b for water droplet impacts ($We = 70$) onto pillars with an intermediate surface wettability ($\theta \approx 73.7°$). The curve progression of $d^*$ over the non-dimensional time $\tau = tU/D_d$ can be directly related to the observed impact morphology. For the curves summarized with (1) ground spreading was observed. The droplet liquid flows around the pillar, encloses it and continues to spread radially on the solid target surface. After reaching $d^*_{max}$ a receding motion is observed. The curves summarized with (2) represent umbrella spreading cases. Here $d^*_{max}$ is smaller in comparison with the ground spreading cases and the receding motion slower, which results from the lamella spreading in air and not along a solid surface.

## Conclusion

We experimentally investigated the droplet impact onto a free-standing cubic surface element with varying size and surface wettability. A change in impact morphology from ground spreading to umbrella spreading was observed when the pillar size is in the order of or larger than the droplet diameter. The temporal evolution of the spreading factor is strongly affect by both pillar size and surface wettability. To gain a better understanding of the effects a more detailed analysis will be conducted in the future.

## Acknowledgments

The authors would like to thank the Deutsche Forschungsgemeinschaft (DFG) for the financial support of the project GRK 2160 "Droplet Interaction Technologies" (DROPIT), under project number 270852890.

## Nomenclature

| | |
|---|---|
| $D_d$ | diameter of impacting droplet [m] |
| $d_s$ | spreading diameter [m] |
| $d^*$ | spreading factor, $d_s/D_d$ [-] |
| $d^*_{max}$ | maximum spreading factor, $d_{s,max}/D_d$ [-] |
| $L_D$ | pillar edge length [m] |
| $\bar{L}_D$ | drop-pillar ratio, $L_p/D_d$ [-] |
| $t$ | time [s] |
| $U_d$ | velocity of impacting droplet [m/s] |
| $\theta$ | contact angle [°] |
| $\tau$ | non-dimensional time, $(tU_d)/D_d$ [-] |

## References

[1] P. Foltyn, D. Ribeiro, A. Silva, G. Lamanna, and B. Weigand. Influence of wetting behavior on the morphology of droplet impacts onto dry smooth surfaces. *Physics of Fluids*, 33(6):063305, 2021.

[2] W. Ren, P. Foltyn, A. Geppert, and B. Weigand. Air entrapment and bubble formation during

droplet impact onto a single cubic pillar. *Sci. Rep.*, 11(1):18018, 2021.

[3] R. Rioboo, M. Marengo, and C. Tropea. Time evolution of liquid drop impact onto solid, dry surfaces. *Experiments in Fluids*, 33(1):112–124, 2002.

# Experimental and numerical investigation of particle-droplet-substrate interaction

Nils Janssen[1], Uwe Janoske*[1]
Department of Mechanical and Safety Engineering, University of Wuppertal, Germany
*Corresponding author: janoske@uni-wuppertal.de

## Introduction

The impact of water droplets (0.68 – 1.66 mm diameter, velocity between 1-2 m/s) on a non-fixed spherical particle (polymethyl methacrylate (PMMA), diameter 1.55 mm) is studied experimentally and numerically. The particle is positioned on a plane PMMA substrate. The impact of the water droplets (Weber number between 13 and 94) leads to different impact scenarios ranging between lift-off of the particle-droplet system, wetting of the particle as well as deposition of the droplet on the particle. Furthermore, the influence of the eccentricity is studied on the impact phenomena. For the numerical modelling, an immersed boundary method is applied to study the impact on the free moving particle which is implemented as an immersed body whereas the droplet is modelled with a Volume-of-Fluid method (VoF).

## Material and methods

The droplet impact on a plane PMMA plate was studied experimentally by using a syringe to produce water droplets between 0.68 and 1.66 diameter. The impact velocity on the PMMA particle (diameter 1.55) which was positioned on the PMMA plate was varied by using different heights. The impact was observed with two high speed cameras used to extract the positions of sphere and droplet as well as the contact angles and length of contact lines. The eccentricity of the impact was detected as well. Due to approx. 50 experiments for one droplet size, the influence of the eccentricity was studied as well. Details of the set-up, postprocessing of the data are described in detail in [1]. For the modelling of the process, a coupled Volume-of Fluid (VoF) method to describe the two-phase flow and an Immersed Boundary Method (IBM) to calculate the movement of the particle is used. The IB method is implemented in OpenFOAM® as a library allowing to use arbitrary OpenFOAM® solvers (here: interFoam for the VoF-method). Details of the method can be found in [2],[3].

## Results and Discussion

The impact can be characterized by a set of dimensionless parameters, namely the ratio of droplet $d_d$ and particle $d_p$ diameter $\Phi = \frac{d_d}{d_p}$ and the Weber number $We = \frac{\rho_d v_d^2 d_d}{\sigma_d}$ which is based on the droplet velocity $v_d$ just before the impact, the surface tension $\sigma_d$ and the density of the droplet $\rho_d$. Fig. 1 shows the plot of the dimensionless diameter ratio as a function of the Weber number. Four different regimes A-D with a complete lift-off of the particle and droplet (A and B), an attachment of the droplet to the particle (C) and a complete wetting of the particle can be observed and categorized according to the dimensionless numbers. A lift-off can be observed for moderate Weber numbers and a droplet-particle ratio around 1.

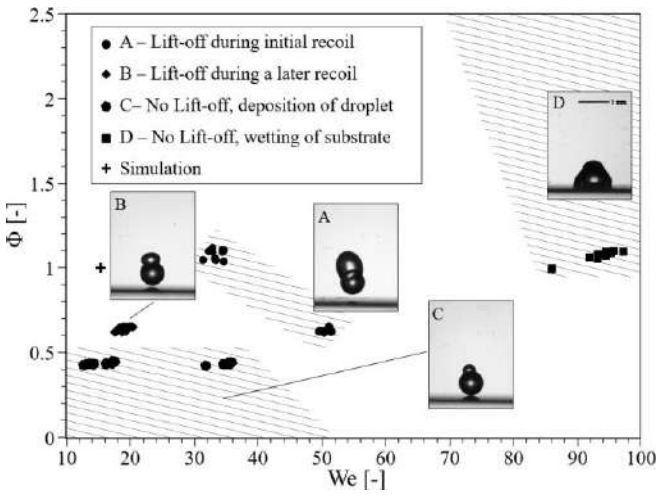


**Figure 1.** Dimensionless ratio droplet and particle diameter $\Phi = \frac{d_d}{d_p}$ as a function of the Weber number *We* for experimental and numerical results

Fig. 2 shows a comparison of the experimental and numerical results for a lift-off scenario for a droplet-particle ratio $\Phi$ =0.91 and a Weber number *We*=13 for different times. The numerical model can predict the scenario of the lift-off (see comparison in Fig. 1) as well as the temporal behaviour of the impact and the lift-off.

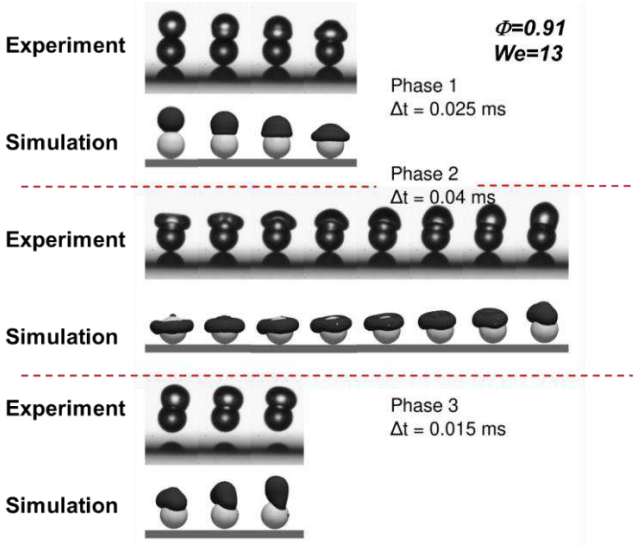


**Figure 2.** Comparison of experimental (top) and experimental (bottom line) results for different times for *We*=13 and $\Phi = 0.91$

**Nomenclature**

| | |
|---|---|
| $d_d$ | Droplet diameter [m] |
| $d_p$ | Particle diameter [m] |
| $v_d$ | Droplet velocity [m/s] |
| *We* | Weber number [-] |
| $\rho_d$ | Droplet density [kg/m³] |
| $\sigma$ | Surface tension [N/m] |
| $\Phi$ | Ratio of droplet and particle diameter [-] |

**References**

[1] Janssen, N., Fetzer, J.R., Grewing, J., Burgmann, S., Janoske, U., Experiments in Fluids 64(44) (2023)
[2] Braschke, K.O., Zoller, J., Freese, F., Dittler, A., Janoske, U., Powder Technology 405(9):117494 (2022)
[3] Zargaran, A., Dolshanskiy, W., Stepanyuk, Pauer, W., Janoske, U., Chemical Engineering Journal, 473, 145062, (2023)

# Spray injection and development realizations and investigations of the effect of droplets coalescence and recirculation on ensemble-averaged predicted data

C.A. Chasos*
Associate Professor, Frederick University, Cyprus
*Corresponding author: c.chasos@frederick.ac.cy

**Introduction**

The recent unfavorable climate change phenomena are enhanced by transport emissions, and cleaner engines with the improvement of engine performance are required. For the development of engines using conventional fossil fuels, as well as alternative liquid and gas fuels, it is required to employ accurate modeling and simulation methodologies, along with realistic initial and boundary conditions, in order to predict the in-cylinder fuel injection, air-fuel mixing, combustion characteristics and emissions. For diesel and gasoline internal combustion engines, high-pressure injectors are employed in direct-injection common rail systems, which result in sprays which may lead to non-premixed, or partially-premixed or premixed in-cylinder combustion. The fuel injection process and the development of spray produces a wide range of droplet sizes and velocity distributions, which affect the air fuel-mixing, thus the various accompanying phenomena require further understanding especially the averaging of data imposed by the ensemble-average of the turbulence modelling closure approach. Computational fluid dynamics (CFD) modelling and simulations of Eulerian/Lagrangian two-phase flow, along with validation of predicted spray data for a wide range of operating conditions are crucial, including various injection pressure and chamber temperatures and pressures conditions. The main objective of the present work is to assess the effect of the number of spray realisations on droplet size and spray penetration, as well as assess the spray droplets coalescence and recirculation phenomena for simulations and their prediction against measured data.

**Methodology**

In the present work, the Eulerian-Lagrangian modelling methodology was employed for the simulation of direct-injection (DI) diesel and gasoline sprays. The overall engine simulation including spray injection, air-fuel mixing, as well as the preparation of combustible mixture are validated against experimental data, in order to assess the validity of the modelling methodology used. The validation framework requires to assess the characteristics of the single-pulse predicted spray against ensemble-averaged estimated from multiple-pulse predicted sprays. Furthermore, the present work accounts for the spray droplet raw data measurements over around 1000 injection pulses, placing emphasis on droplet size data scatter, ensemble-averaged data and the standard deviation.

The Eulerian-Lagrangian included the governmental equations of the gas phase (Eulerian approach) and liquid phase (Lagrangian approach), the turbulence modelling of the gas phase (k-ε high Reynolds number and variants), spray atomization modelling (Reitz-Diwakar spray atomisation model for diesel spray and the variant of Taylor Analogy breakup for gasoline spray (Model A)), the Reitz-Diwakar droplet break-up model and O'Rourke inter-droplet collision model for injector type) were employed. For the spray simulations, the differencing scheme MARS was employed and the conjugate gradient algorithm was used. For the simulations of the present work, sensitivity studies of the key numerical parameters, namely mesh size, time step size and parcel introduction rate have been performed.

**Results and discussion**

Two case studies with spray simulation and validation investigations are presented, namely a DI diesel spray (for pure diesel and biodiesel injection), and a DI gasoline spray for single and multiple pulses assessment. First, the case study of DI diesel injector simulations with two different fuels, namely pure diesel (B0) and pure biodiesel (B10) are presented, including spray pattern qualitative comparisons against photgraphs and spray penetration validation. Second, the DI gasoline spray simulations are compared against photographs and spray penetration simulations are compared against measured penetration. It is emphasized that the experimental data considered a number of spray realisations, while the simulation data was from a single pulse simulation. Since experimental data of size and penetration deviations from pulse to pulse were not available, then droplet size raw data was utilised for estimating deviation.

For case study of DI gasoline spray, the number of spray realisations was assessed for a statistically representative number of injection pulses, notably 30 injection pulses of spray simulations using different random sizes of droplets from the same droplet size distribution employed in the DI gasoline atomization model.

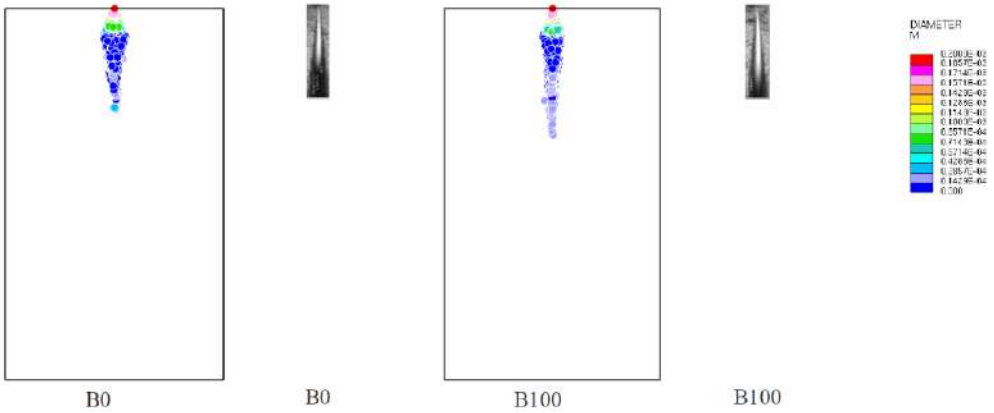


**Figure 1.** Diesel (B0) and biodiesel (B100) spray simulations comparison with photographs in high pressure (42 bar) and temperature (1000 K) chamber at 1.5 ms ASOI (from [1]).

As it can be seen in Figure 1, the simulated spray produced with biodiesel penetrates further downstream and it is narrower than the simulated spray with pure diesel. The prediction of increased spray penetration with increasing biodiesel blending percentage agrees with the experiment. Figure 2 shows comparisons of spray penetration between the simulations with B0 and B100 and the experimental data. The penetrations from the experiment were measured from the spray photographs at 1.5 ms after start of injection (ASOI). The penetration definition for the simulation was set as the vertical line to the nozzle symmetry line, behind which the 90% of the total mass of injected spray droplets resides. For both test fuels, spray penetration is slightly overpredicted and is in good agreement with the trend observed in the experiment, where biodiesel penetration is longer than diesel penetration.

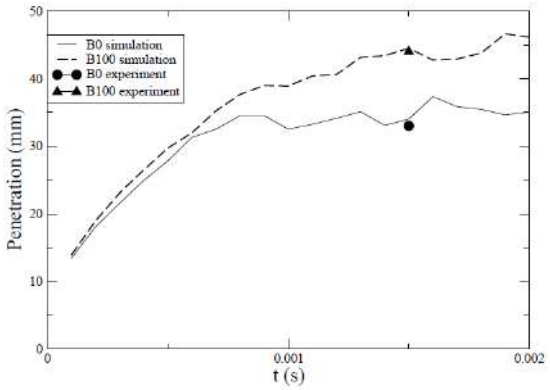


**Figure 2.** Diesel (B0) and biodiesel (B100) spray penetration comparisons for high pressure (42 bar) and temperature (1000 K) chamber (from [1]).

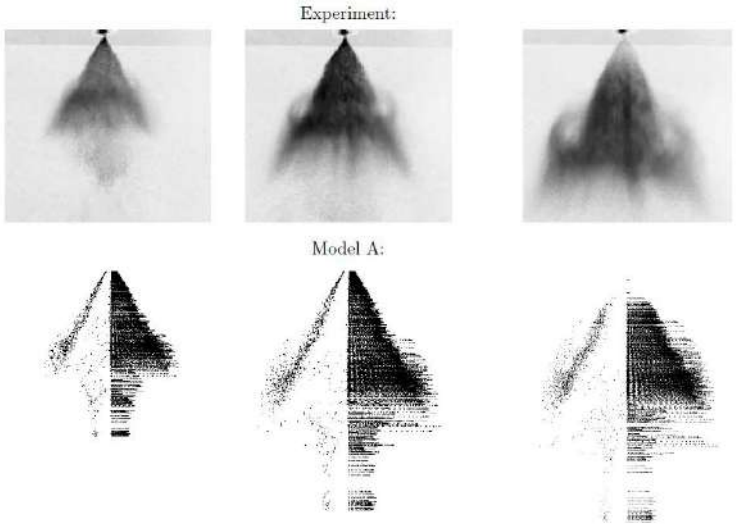


**Figure 3.** Gasoline spray simulation comparison with spray photographs at 0.8, 1.2 and 1.5 ms ASOI for injection pressure 70 bar at atmospheric chamber (from [2]).

For the DI gasoline spray, comparisons of the spray simulation against spray photographs are presented in Figure 3 at elapsed time ASOI. It can be seen that the simulation predicts the shape and structure of the spray, and the droplets' recirculation zones at the outer region of the spray are correctly captured. Therein, clustering and coalescences of droplets may occur which affect the spray penetration and the droplet size as it is explained below.

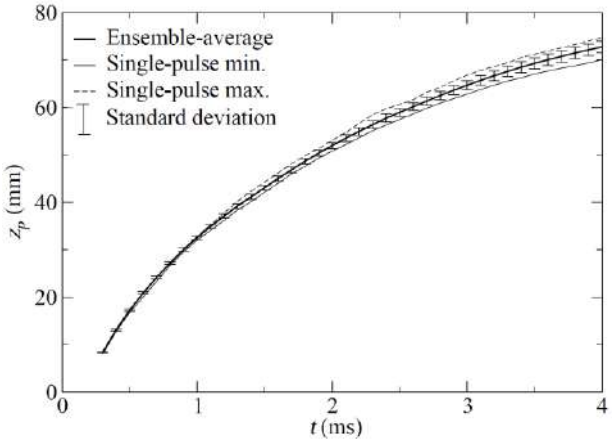


**Figure 4.** Gasoline spray penetration simulation comparison with standard deviation bars for single pulse minimum and maximum penetration and ensemble-average penetration from multiple pulses, for injection pressure 70 bar at atmospheric chamber (from [2]).

Figure 4 shows the penetration of spray as function of time from the number of realisations investigation. It can be seen that until 1 ms ASOI the differences of the single pulse data and the ensemble-averaged data are negligible. The single-pulse data fluctuates around the ensemble-average data. However, with elapsed time the minimum and maximum penetration from single pulses show increasing difference, which can be attributed to the decreasing droplet size, and the enhanced recirculation and coalescence of droplets.

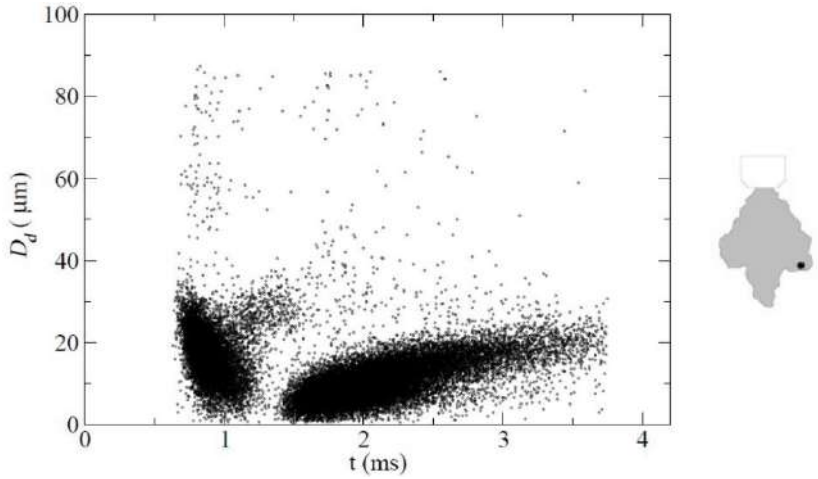


**Figure 5.** Raw droplet size data from multiple-pulse PDA local measurement (z=25mm, r=13mm), for injection pressure 70 bar at atmospheric chamber (from [2]).

Figure 5 illustrates experimental measurement of droplet diameter with the phase Doppler anemometry (PDA) technique. On the right side of Figure 5, the location of the measurement is provided in a schematic diagram which shows the injector tip and the spray pattern. The location was 25 mm axial distance from the nozzle exit and 13 mm radial distance from the nozzle symmetry axis. At around 1.3 ms ASOI, there is limited droplet data recorded, presented as a data gap, either because of the dense spray or because the main body spray and droplets cluster have passed the measurement location. From Figure 5, it can be observed that bigger droplets are measured at the early stages of spray injection and at later time at around 1.5 ms ASOI smallers droplet are captured, and there is a trend to accumulate because of recirculation which may create an increased size of droplets after 2 ms ASOI. The amount of droplets captured after 3 ms ASOI is decreasing, which reveals that the spray clustering and droplets that are recirculating travel far downstream.

The raw droplet size data from Figure 5, which was recorded with PDA over around 1000 injection pulses during the experimental measurement was ensembled-averaged, and the standard deviation of the droplet diameter was estimated and it is presented in Figure 6. In Figure 6, it can be observed that smaller droplets are measured after 1.5 ms ASOI and size deviation decreases with elapsed time. This might be explained by the fact that small droplets can be affected by the gas motion, and these are recirculating and remaining at the vicinity of the measurement location for longer period than 3 ms.

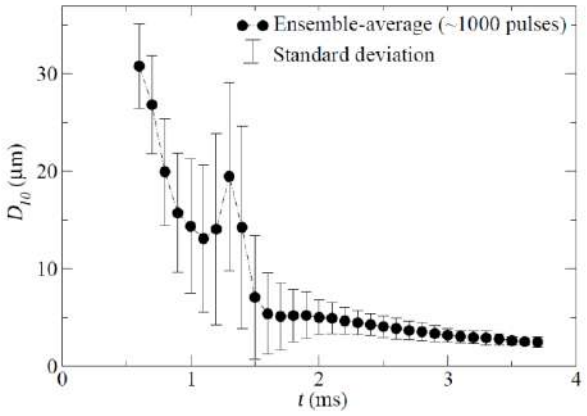


**Figure 6.** Ensemble-average and standard deviation of droplet diameter data from multiple-pulse PDA local measurement (z=25mm, r=13mm), for injection pressure 70 bar at atmospheric chamber (from [2]).

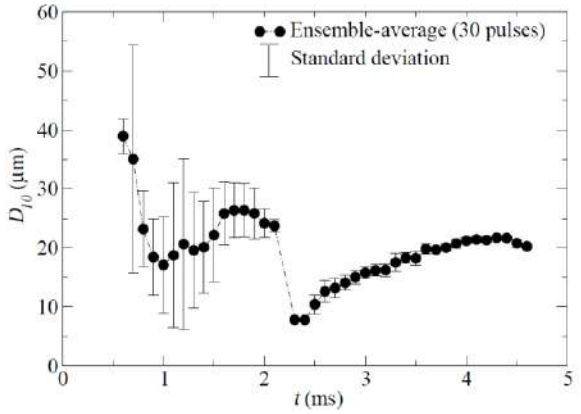


**Figure 7.** Ensemble-average and standard deviation of droplet diameter data from multiple-pulse CFD simulations (z=25mm, r=13mm), for injection pressure 70 bar at atmospheric chamber (from [2]).

Figure 7 includes the ensembled-averaged and the standard deviation droplet diameter data estimated from the multiple-pulse spray simulations for 30 different spray pulses. At the initial stages of spray injection, when the droplets arrive at the location for averaging, big droplets are predicted and the deviation of droplet size is relatively high. Also, a similar finding to the finding of experimental data is reached, which reveals that droplet size deviation becomes negligible during the later stages of spray injection at the particular location.

**Conclusions**

The experiment can provide raw data, where randomness exists, for example in the injector operation (needle opening and closing), the atomisation process, and the flow field interactions due in part to the turbulence. The spray measured at each injection pulse is different, and the difference in spray penetration and droplet size can be characterized with standard deviation resulting from big amount of measured data. In spray simulations of the kind which were considered in the present work, the Navier-Stokes equations are ensemble-averaged, while the Lagrangian spray equations are not ensemble-averaged, therefore a single spray pulse may in principle be not sufficient to describe the stochastic spray behavior, thus a representative number of spray realisations could be required. Scatter and deviations of data should be considered for spray validation studies.

**References**

[1] Chasos, C. A., Christodoulou, C. N. and Karagiorgis, G. N. “CFD simulations of multi-hole Diesel injector nozzle flow and sprays for various biodiesel blends”. Proceedings of ICLASS 2012, 12th Triennial International Conference on Liquid Atomization and Spray Systems, Heidelberg, Germany, September 2-6, 2012. (Paper ref. No. 1263).

[2] Chasos, C. A. “Computational fluid dynamics simulation of direct injection gasoline sprays”. PhD thesis, Imperial College of Science Technology and Medicine, University of London, England, 2006.

# Evaporation of an oscillating drop

Y. Hu*[1], S. Tonini[1], G.E. Cossali[1], B. Weigand[2], J. Reutzsch[2], M. Frey[2]

[1]Dipartimento di Ingegneria e Scienze Applicate, Università degli studi di Bergamo, Italy
[2]Institute of Aerospace Thermodynamics, University of Stuttgart, Germany
*Corresponding author: yueqiao.hu@unibg.it

## Introduction

The study of droplet dynamics has a long history due to its wide application in different fields, such as spray coating, fire suppression, aero-engine, pharmacology, etc.[1]. Much work has been done in drop evaporation[7, 3] and oscillation[8, 4], respectively. However, in most scenarios, these both proceed simultaneously and have an effect on the other one. Until now, only few papers[5, 6] referred to the evaporation of an oscillating droplet. In the present work, we consider the evaporation of an oscillating droplet, releasing the assumption of quasi-steady heat and mass diffusion into the gas phase. The conservation equations were solved by numerical methods using an in-house code (FS3D). The distribution of vapour flux of a spheroidal droplet at the droplet surface under oscillating conditions is discussed and compared with the results of a droplet under quasi-steady conditions.

## Numerical approach

We ran the simulations using an in-house code (FS3D), which was developed for DNS of incompressible multiphase flows with sharp interfaces between immiscible phases. FS3D solves the incompressible Navier-Stokes equations as well as the energy equation for the phase transition. The interface reconstruction is realized by VOF and PLIC methods. Without any turbulence model, FS3D is able to resolve the smallest temporal and spatial scales by DNS. However, it requires large computational efforts, which could be met by employing OpenMP as well as MPI[2].

## Formulation of the problem

We consider a droplet oscillating in a gaseous environment. The computational domain is shown in Figure 1, a spheroidal water droplet of initial semi-axis $a_r = 0.5mm$, $a_z = 0.6mm$ oscillates and evaporates in the air, in the middle of the domain, which has the dimensions $2.8mm \times 2.8mm \times 2.8mm$ (grid resolution $128 \times 128 \times 128$). All boundaries have continuous conditions. The surface tension coefficient, liquid dynamic viscosity, and vapour-air diffusivity coefficient are set to $76.40mN/m$, $0.003Pa \cdot s$, and $28.45 \times 10^{-6} m^2/s$, respectively. The ambient pressure is set at $0.965 \times 10^5 Pa$. The initial air temperature is $351K$, while the drop temperature is $350.8K$. The small temperature difference is chosen to decrease the influence of the initial temperature difference on the vapour concentration distribution and the computational cost.

The ratio of evaporation time scale $t_{ev} \propto \frac{R_d^2}{D}$ and oscillation time scale $t_{osc} \propto \sqrt{\frac{\rho R_d^3}{\sigma}}$ is defined as the parameter $\phi = \frac{t_{ev}}{t_{osc}}$. For drop oscillations without evaporation, the parameter $\phi$ goes to infinite. For the evaporation of spheroidal droplets under a quasi-steady assumption, the parameter $\phi$ nears to be zero. In the present work of an evaporating and oscillating drop, the parameter $\phi$ is about 7. Thus the release of the quasi-steady assumption is expected to yield different results.

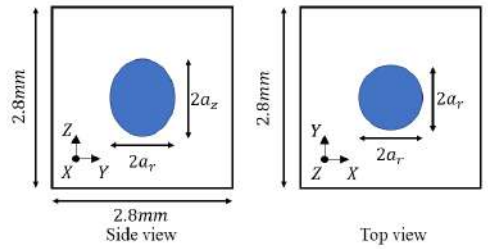


**Figure 1.** Computational domain of setup

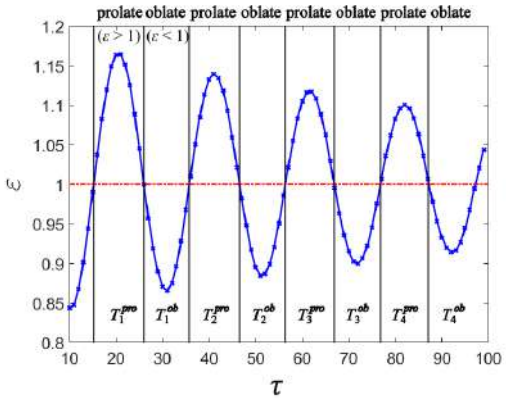


**Figure 2.** Aspect ratio with respect to time

**Table 1.** Time spent by droplet in the prolate and oblate shape.

| | time in prolate shape (ms) | time in oblate shape (ms) | percentage of time in prolate shape (%) |
|---|---|---|---|
| period 1 | $T_1^{pro}: 1.641$ | $T_1^{ob}: 1.531$ | 51.73 |
| period 2 | $T_2^{pro}: 1.605$ | $T_2^{ob}: 1.572$ | 50.52 |
| period 3 | $T_3^{pro}: 1.588$ | $T_3^{ob}: 1.561$ | 50.43 |
| period 4 | $T_4^{pro}: 1.576$ | $T_4^{ob}: 1.544$ | 50.51 |

## Results and Discussion

In this section, the numerical results are presented and discussed. The decay of aspect ratio $\varepsilon = \frac{a_z}{a_r}$ is depicted in Figure 2, $\tau$ is defined as $\tau = \frac{\Delta t}{t}$ with $\Delta t = 0.154ms$. $\varepsilon > 1$ corresponds to a prolate shape, $\varepsilon < 1$ represents an oblate shape. Table 1 records the time spent by the droplet in the prolate or oblate shape in different periods. The time spent in prolate shape decreases with the period, the leap of time in oblate shape in the second period may be due to the initial instability. Figure 3 shows the velocity and temperature field in the XY and YZ plane at time $\tau = 44$ when the droplet has a prolate shape and $\varepsilon$ is decreasing. No vortex flow inside the droplet is observed due to the small scale of the droplet. The temperature gradient across the interface is high due to the vaporization.

The spatial distribution of vapour flux of an oscillating droplet at the droplet surface shows different characteristics from that of a droplet under quasi-steady conditions. $\eta$ is the cosine of the polar angle of an arbitrary position at the droplet surface, $\eta = 0$ represents the equator and $\eta = 1$ or $-1$ is the upper or lower pole. As shown in Figure 4 (a), the dimensionless vapour flux $\hat{\xi} = \frac{\xi}{\frac{\dot{m}_{ev}}{4\pi R_0^2}}$ in unsteady conditions reaches a higher value both at the equator and poles, regardless of the droplet shape. However, according to[9], the vapour flux $\xi$ of a spheroidal droplet under quasi-steady conditions is expressed as $\xi = (R_0^2 K_G)^{1/4} \frac{\dot{m}_{ev}}{4\pi R_0^2}$. The dimensionless vapour flux $\hat{\xi}$ is proportional to the dimensionless Gauss curvature to the quarter power. Figure 4 (b) shows the distribution of the dimensionless vapour flux of a spheroidal droplet under quasi-steady conditions. It reaches a higher value at the equator for the oblate shape, while at the poles for the prolate shape.

By the way, the effect of diffusivity and viscosity is shown in Figure 5. Diffusivity in test 1, test 2, and test 3 are 28.45, 28.45, and $50 \times 10^{-6} m^2/s$, respectively. Viscosity in test 1, test 2, and test 3 are 0.003, 0.005, and 0.005 $Pa \cdot s$, respectively. The difference between test 2 and test 3 is negligible. The higher viscosity suppresses the oscillating amplitude, and the higher diffusivity has almost no effect.

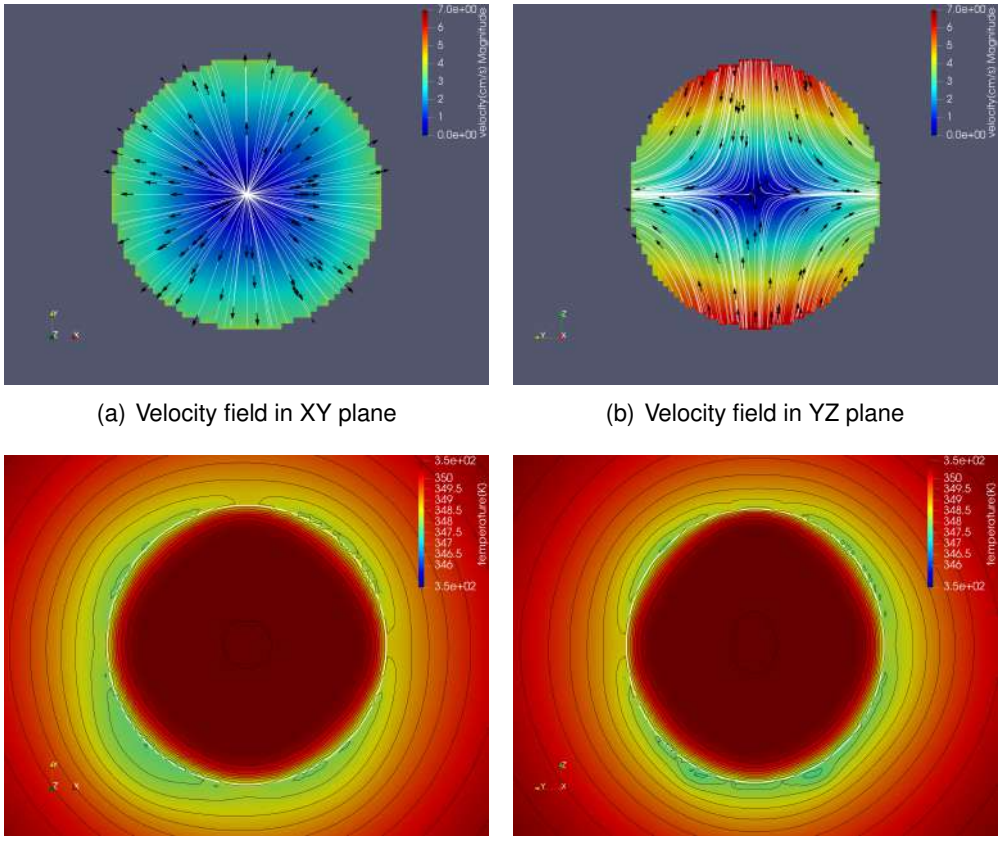


(a) Velocity field in XY plane

(b) Velocity field in YZ plane

(c) Temperature field in XY plane

(d) Temperature field in YZ plane

**Figure 3.** Velocity and temperature field in the XY and YZ plane.

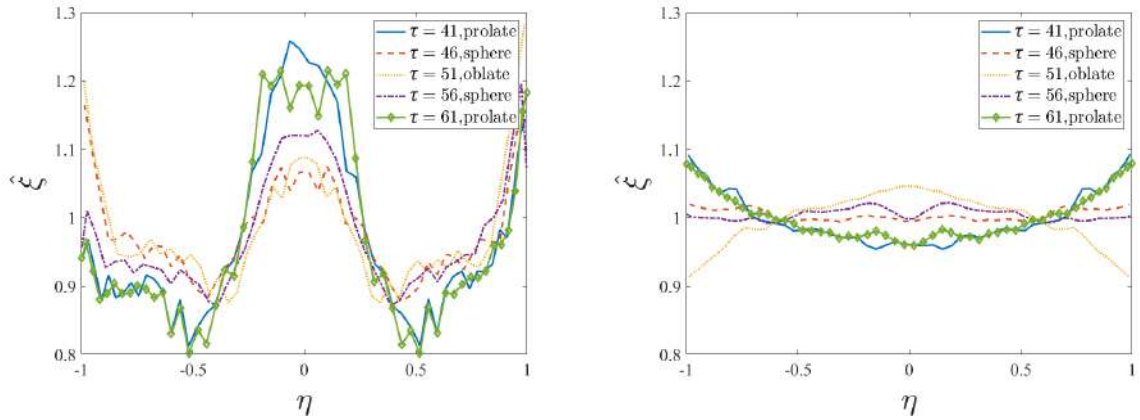


(a) Spatial distribution of vapour flux under unsteay conditions in one period, from simulation results($\phi = \frac{t_{ev}}{t_{osc}} \simeq 7$)

(b) Spatial distribution of vapour flux under quasi-steady conditions in one period, from theoretical results according to [9] ($\phi = \frac{t_{ev}}{t_{osc}}$ nears to be zero)

**Figure 4.** Comparison of spatial distribution of vapour flux under unsteady and quasi-steady conditions.

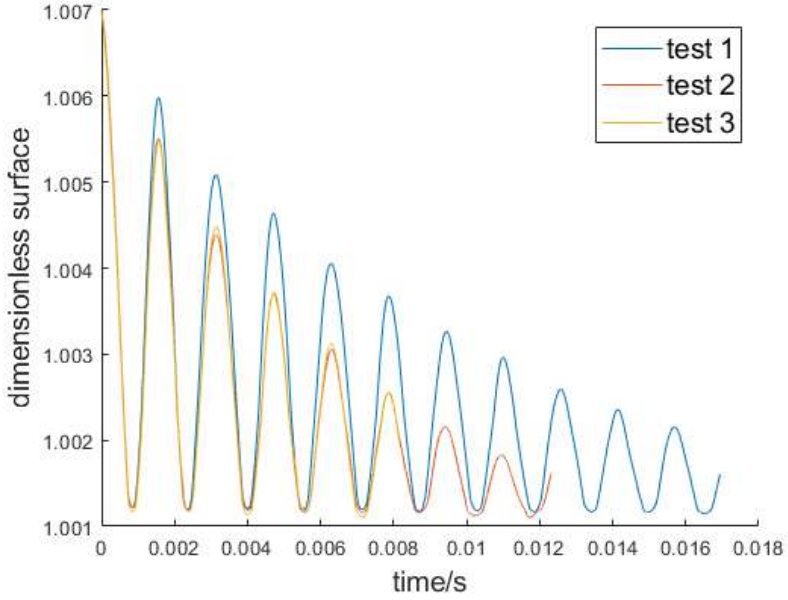


**Figure 5.** Effect of diffusivity and viscosity

## Conclusion

An oscillating droplet under evaporating conditions is numerically investigated. The vapour flux of a droplet under unsteady conditions shows different characteristics from that of a droplet under quasi-steady conditions. It reaches a higher value at the equator and the poles at any moment, regardless of the droplet shape. The temperature has a high gradient across the interface due to the vaporization. The higher viscosity suppresses the oscillation amplitude, and the higher diffusivity has no effect. These findings urge a deeper analysis on the effect of taking into account the non-quasi steadiness on the modelling of evaporation of oscillating droplets.

## References

[1] G. Brenn and S. Teichtmeister. Linear shape oscillations and polymeric time scales of viscoelastic drops. *Journal of fluid mechanics*, 733:504–527, 2013.

[2] K. Eisenschmidt, M. Ertl, H. Gomaa, C. Kieffer-Roth, C. Meister, P. Rauschenberger, M. Reitzle, K. Schlottke, and B. Weigand. Direct numerical simulations for multiphase flows: An overview of the multiphase code fs3d. *Applied Mathematics and Computation*, 272:508–517, 2016.

[3] N. A. Fuchs. *Evaporation and droplet growth in gaseous media*. Elsevier, 1959.

[4] H. Lamb. On the oscillations of a viscous spheroid. *Proceedings of the London Mathematical Society*, 1(1):51–70, 1881.

[5] F. Mashayek. Dynamics of evaporating drops. part i: formulation and evaporation model. *International journal of heat and mass transfer*, 44(8):1517–1526, 2001.

[6] F. Mashayek. Dynamics of evaporating drops. part ii: free oscillations. *International journal of heat and mass transfer*, 44(8):1527–1541, 2001.

[7] J. C. Maxwell. Diffusion. *Encyclopedia britannica*, 7(214):625–646, 1878.

[8] L. Rayleigh et al. On the capillary phenomena of jets. *Proc. R. Soc. London*, 29(196-199):71–97, 1879.

[9] S. Tonini and G. Cossali. An exact solution of the mass transport equations for spheroidal evaporating drops. *International Journal of Heat and Mass Transfer*, 60:236–240, 2013.

# Relation Between Shear Rate and Structural Parameter in Non-Newtonian Droplet Oscillations via Jacobi Sets and STL Decomposition: A Visual Analysis

D. Klötzl*[1], M. Ibach[2], B. Weigand[2], D. Weiskopf[1]
[1]Visualization Research Center (VISUS), University of Stuttgart, Stuttgart, Germany
[2]Institute of Aerospace Thermodynamics (ITLR), University of Stuttgart, Stuttgart, Germany
*Corresponding author: daniel.kloetzl@visus.uni-stuttgart.de

**Keywords**
DNS, VOF, Multiphase, Droplet Oscillation, Non-Newtonian, Thixotropy, Jacobi Sets, STL

**Introduction**
Liquids with a non-Newtonian rheological behavior are frequently encountered in engineering applications, such as coating, polymer processing, and oil drilling. Thixotropy is a scarcely investigated non-Newtonian behavior in which the fluid's viscosity depends on the shear rate and the deformation history. Understanding the rheological behavior of thixotropic fluids is essential in applications, but it is challenging to quantify and examine involved processes and mechanisms separately in experiments. Therefore, numerical simulation can be used to characterize and quantify the fluid behavior.
The main objective of this work is to reveal the relationships between the fluid structure and the flow field inside a thixotropic fluid droplet by analyzing data of the fundamental case of an oscillating droplet consisting of an ideal thixotropic fluid. To this end, we use the in-house multiphase flow solver Free Surface 3D (FS3D) [1,2]. The analysis is conducted with the two methods: Jacobi sets, introduced by Edelsbrunner et al. [3], a mathematical tool that captures gradient alignments of multiple scalar fields, and seasonal-trend decomposition based on loess (STL) by Cleveland et al. [4], a method used to analyze and extract trends and seasonal patterns in time series data.
The first goal of this study is to investigate the interdependence of shear rate and structural parameter, which characterizes the integrity of the thixotropic fluid, using the improved Jacobi set computation method by Klötzl et al. [5, 6] to better understand the governing processes. The second goal is to use STL decomposition to analyze and extract trends and seasonal patterns for different parameters that control the recovery and breakdown of the fluid structure. The tools in this study can be used to present data from the parametric study and expose fundamental connections between the fluid structure and flow field. Moreover, the methods introduced here can be applied to derive appropriate correlations essential for designing and optimizing various industrial processes involving thixotropic fluids.

**Dataset and Methods**
The numerical modeling of the evolution of the structural parameter $\lambda$ is computed via the transport kinetic equation

$$\underbrace{\frac{\partial \lambda}{\partial t} + u \cdot \nabla \lambda}_{Advection} = \underbrace{-k_1 \dot{\gamma} \lambda}_{Breakup} + \underbrace{k_2 (1 - \lambda)}_{Rebuilding}, \quad (1)$$

introduced by Moore [7], in combination with the constitutive equation for the viscosity

$$\eta_a(\lambda) = \eta_\infty (1 + \alpha \lambda), \quad (2)$$

using FS3D, see [2]. Here, the structural parameter $\lambda$ varies between 0 and 1, where $\lambda = 0$ corresponds to a completely broken and $\lambda = 1$ to a fully recovered microstructure. The shear rate is denoted via $\dot{\gamma}$, the breakdown strength and recovery rate are given via $k_1$ and $k_2$, respectively. For the apparent viscosity $\eta_a(\lambda)$ that is linked to the infinite shear viscosity $\eta_\infty$ and the zero-shear viscosity $\eta_\infty(1 + \lambda)$, the special cases of $\alpha = 0$ (no effect on the viscosity of the droplet) and $\alpha = 99$ (a link between the structural parameter and the droplet's viscosity) are investigated. We compare different configurations of the non-dimensional parameters $k_1$ and the mutation number $\mathrm{Mu} = k_2 \cdot T_{sim}$ with the oscillation period of the droplet used as a characteristic time scale.
For the visual analysis, we use the Jacobi set and STL separately. In the special case of two-dimensional scalar-valued functions $\mathrm{f}, \mathrm{g} \in \mathbb{R}^2 \supset M \to \mathbb{R}$, the Jacobi set can be defined via $J(f, g) \coloneqq \{x \in M : \nabla \mathrm{f} \times \nabla \mathrm{g} = 0\}$, thus it captures gradient alignments of given scalar fields. In the second analysis, the time series was decomposed additively into a trend, seasonal (according to the period $T_{sim}$), and residual component. This decomposition is illustrated for the example of the evolution of the structural parameter $\lambda$ over the non-dimensional time for $k_1 = 10$ (blue) and $k_1 = 40$ (red) in Figure 1.

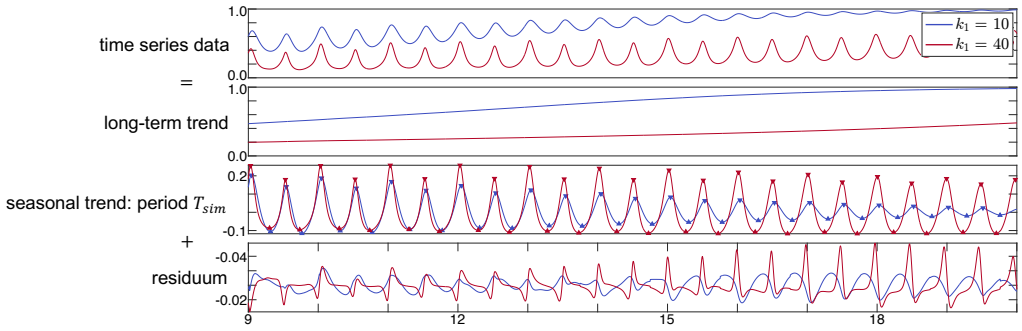


**Figure 1.** STL decomposition of the evolution of the structural parameter $\lambda$ over the non-dimensional time $\tilde{t} = t/T_{sim}$ for $k_1 = 10$ (blue) and $k_1 = 40$ (red), $Mu = 10$ with highlighted min/max in the seasonal component.

**Results and Discussion**

In Figure 2, the droplets are given at time $\tilde{t} = 0.43$ (top) and $\tilde{t} = 2.43$ (bottom). The shear rate $\dot{\gamma}$ and the structural parameter $\lambda \in [0,1]$ for $Mu = 10$ are used as the two input scalar fields for the Jacobi set for the cases of $k_1 = 10$ (left) and $k_1 = 0.1$ (right). The corresponding scalar fields are visualized via two colormaps in the background and the current flow field inside the droplet via line integral convolution (LIC) [8]. The Jacobi sets (black/white lines) for these specific time steps differ for different $k_1$ values. The comparison of the numerical results reveals that the Jacobi sets show similar results in two-thirds of the regarded time steps. From this exploration, an analytic investigation of the Jacobi set dependence between the structural parameter and the shear rate could lead to an analytic dependence. Another possible research direction could be the analysis of the interdependence between Jacobi set and varying $k_1$ and $Mu$ values of the breakup and rebuilding of the fluid structure.

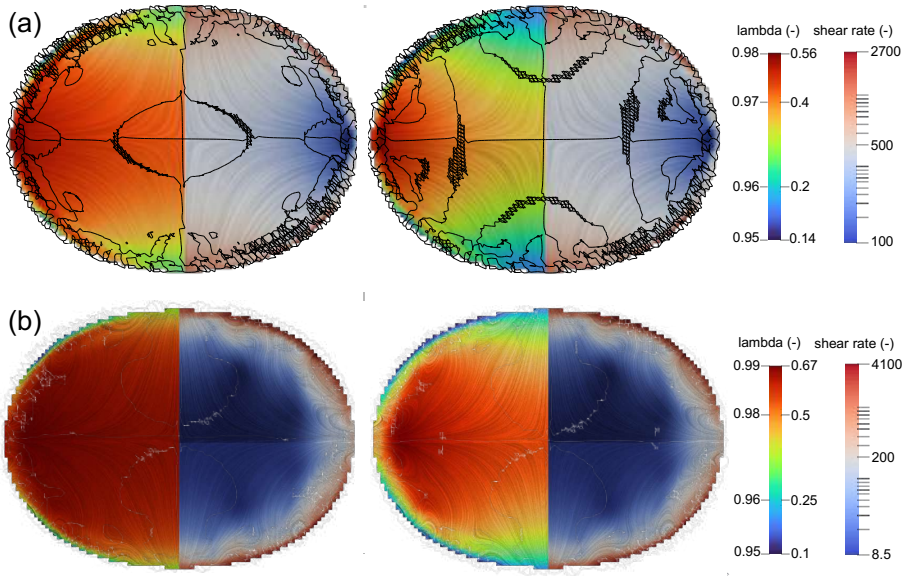


**Figure 2.** Jacobi set (black/white lines) of the shear rate $\dot{\gamma}$ and the structural parameter $\lambda \in [0,1]$ for $Mu = 10$: (a) at time $\tilde{t} = 0.43$ for $\alpha = 0$ (left: $k_1 = 10$, right: $k_1 = 0.1$) and (b) at time $\tilde{t} = 2.43$ for $\alpha = 0$ (left: $k_1 = 10$, right: $k_1 = 0.1$).

For the second part, we discuss the results of the decomposition of the averaged structural parameter $\lambda$ using STL. Here, the evolution of the structural parameter $\lambda$ over the non-dimensional time $\tilde{t}$ is decomposed into a trend, seasonal, and absolute residual component. This decomposition is given in Figure 3 for different mutation numbers 0.1 and 10 (on the left) as well as 1 and 100 (on the right) for a range of $k_1$ values between 0.01 and 100. The $k_1$ values are visually encoded using different colors from a discrete warm cold color scale. Furthermore, two detailed zoomed-in areas of the seasonal and residual components of the mutation numbers 1 and 10 are given.

In the analysis, the STL decomposition simplifies the comparison of the oscillation heights between the different configurations since one can directly compare the seasonal patterns to each other. This confirms the results from Ibach et al. [2] that the maxima of the averaged structural parameter $\lambda$ lie ahead of the maxima of the oscillating modes. Moreover, one can state that the higher the breakdown strength $k_1$, the more distinct the shift between the maxima is. This is especially emphasized in the zoomed-in areas for the mutation numbers 1 and 10.

The numerical exact evaluation of the decomposed structural parameter's maxima shift in comparison to the oscillation modes could be of interest for further investigation in the future.

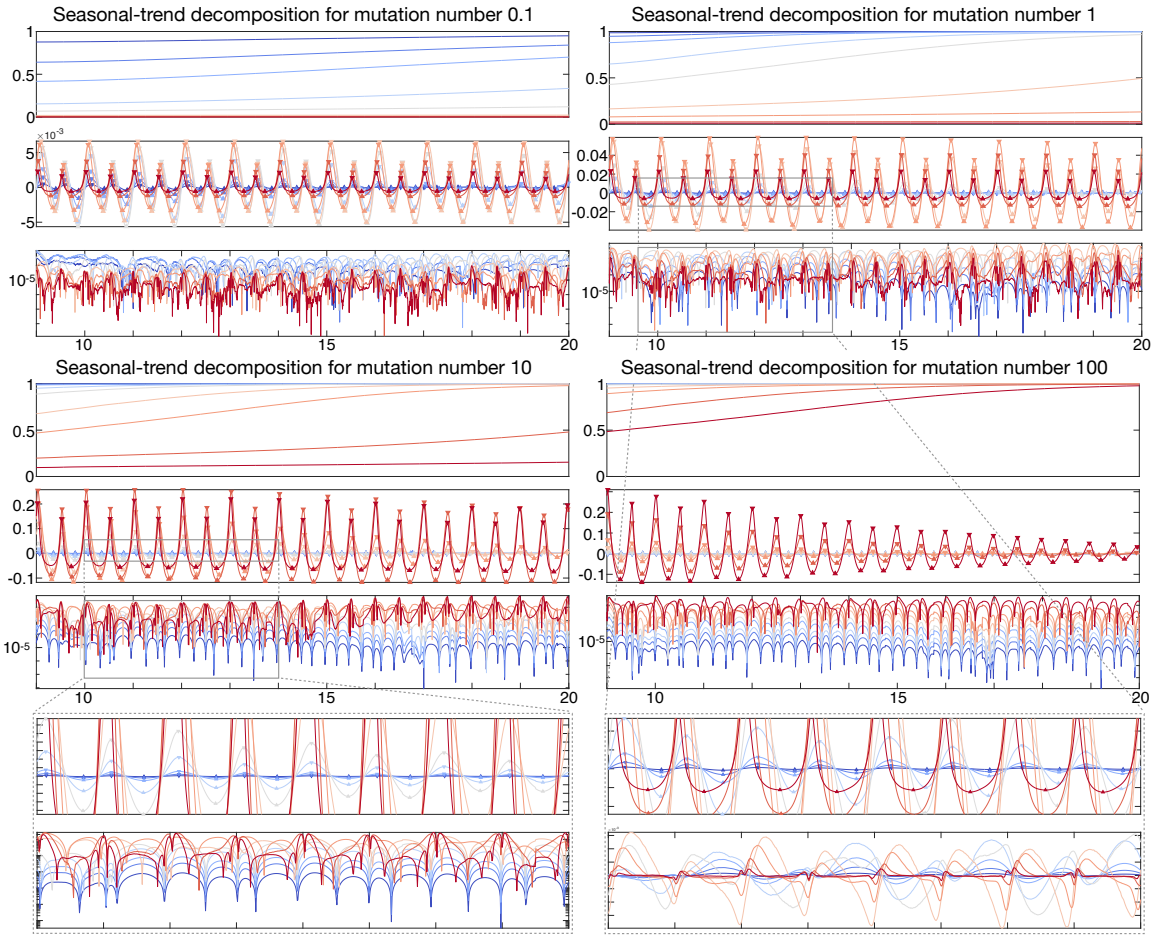


**Figure 3.** STL decomposition of the evolution of the structural parameter $\lambda$ over the non-dimensional time $\tilde{t}$ for the mutation numbers 0.1 and 10 (left) as well as 1 and 100 (right). The different $k_1$ values are visually encoded in the discrete warm cold color scale. Zoomed-in areas highlight two specific regions of the resulting seasonal and residual components (upper and lower part, respectively).

**Acknowledgments**

This work was supported by the Deutsche Forschungsgemeinschaft (DFG, German Research Foundation) – Project-ID 270852890 – GRK 2160/2 and under Germany's Excellence Strategy – EXC 2075 – 390740016. We also acknowledge the support by the Stuttgart Center for Simulation Science (SimTech) and the High-Performance Computing Center Stuttgart (HLRS) for the support and the supply of computational resources on the HPE Apollo (Hawk) platform under Grant No. FS3D/11142.

**References**

[1] K. Eisenschmidt, M. Ertl, H. Gomaa, C. Kieffer-Roth, C. Meister, P. Rauschenberger, M. Reitzle, K. Schlottke, and B. Weigand, "Direct numerical simulations for multiphase flows: An overview of the multiphase code FS3D," Appl Math Comput, vol. 272, pp. 508–517, 2016.

[2] M. Ibach, J. Steigerwald, and B. Weigand, "Thixotropic effects in oscillating droplets," in 11th International Conference on Multiphase Flows, Kobe, Japan, 2023.

[3] H. Edelsbrunner and J. Harer, "Jacobi sets of multiple Morse functions," in Found Comput Math, pp. 37–57, 2002.

[4] R. B. Cleveland, W. S. Cleveland, J. E. McRae, and I. Terpenning, "STL: A seasonal-trend decomposition," J Offic Stat, vol. 6, no. 1, pp. 3–73, 1990.

[5] D. Klötzl, T. Krake, Y. Zhou, I. Hotz, B. Wang, and D. Weiskopf, "Local bilinear computation of Jacobi sets," Vis Comput, vol. 38, no. 9, pp. 3435–3448, 2022.

[6] D. Klötzl, T. Krake, Y. Zhou, J. Stober, K. Schulte, I. Hotz, B. Wang, and D. Weiskopf, "Reduced connectivity for local bilinear Jacobi sets," in 2022 Topological Data Analysis and Visualization (TopoInVis), pp. 39–48, 2022.

[7] F. Moore, "The rheology of ceramic slips and bodies", Trans Br Ceram Soc 58, pp. 470–494, 1959.

[8] B. Cabral and L. C. Leedom, "Imaging vector fields using line integral convolution," in Proceedings of the 20th Annual Conference on Computer Graphics and Interactive Techniques, pp. 263–270, 1993.

# An approach to investigate the 3D height evolution in the crown crater during early crown formation with the General Defocusing Particle Tracking (GDPT) method

Pablo Molina Vogelsang*, Stefan Schubert, Grazia Lamanna
Institute of Aerospace Thermodynamics (ITLR), University of Stuttgart, Stuttgart, Germany
*Corresponding author: pablo.molina-vogelsang@itlr.uni-stuttgart.de

## Introduction

The interaction between droplets and a wall film holds significance in various technical and natural-scientific processes, from raindrops impacting water puddles to industrial engine as a maintenance step. Analyzing the impact of a single drop on a thin liquid film reveals the radial growth of the crown crater and the simultaneous upward expansion of the crown wall. We focus our studies on the elevation phase, which describes the time between impact and maximum crown growth. Many phenomena such as the velocity field in the crown crater region or the 3D height evolution in the crown crater during early crown formation are not yet well understood. In the context of our research, we are developing a method to measure the 3D height evolution in the crown crater of early crown formation using the MATLAB code DefocusTracker (GDPT method) developed by Rossi and Barnkob [1][2]. Therefore, we presented a poster providing an overview of the experimental micro-PTV setup and the fundamentals of the evaluation routine (GDPT). Additionally, we showcased preliminary measurement results, illustrating how 3D information is obtained from a 2D image through the defocusing effect.

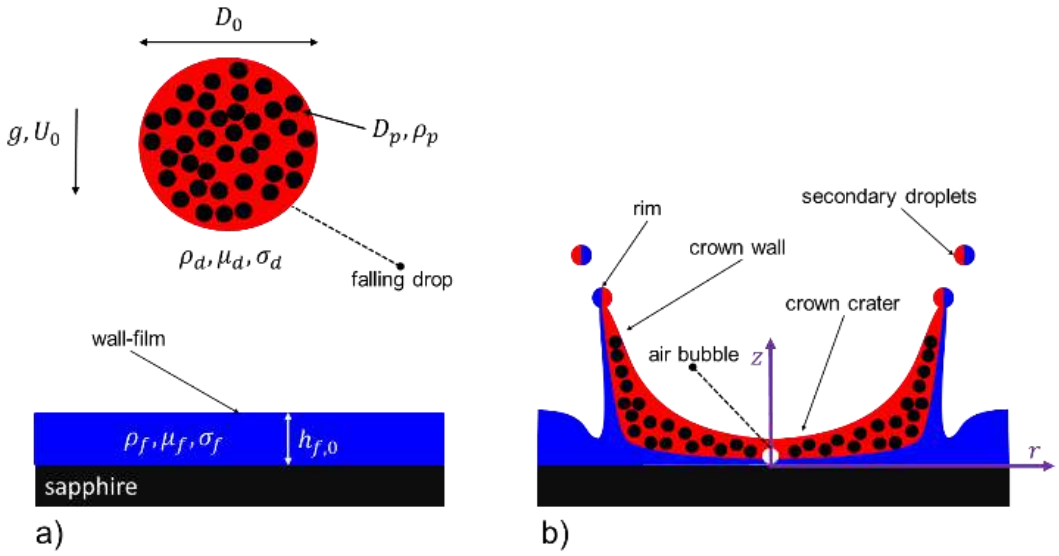


**Figure 1.** a) A single drop $(D_0, U_0, \rho_d, \mu_d, \sigma_d)$ seeded with tracer particles $(D_p, \rho_p)$ falls onto a thin liquid film $(h_{f,0}, \rho_f, \mu_f, \sigma_f)$. b) The outcome: crown formation after the impact. The height evolution in the crown crater is defined by the ordinate $z$ and the radially outward particle trajectories by the abscissa $r$.

## Experimental setup and methods

The main components of the imaging system are an Axio Observer Z1 microscope from Carl Zeiss and two fully synchronized Photron Fastcam SA-X2 high-speed cameras: one for an oblique top view (macro view) and the other for a bottom view (micro view) through the microscope. The cameras are used to capture a series of 12-bit grayscale images with a resolution of 1024 x 1024 px² at a frame rate of 12,500 frames per second. Both views operate in backlight mode. We utilize a high-power LED for shadow graphics, with a color temperature of 6500 K for the oblique top view and 5000 K for the bottom view. Additionally, the experimental setup includes a droplet generation system (the droplet is seeded with Polystyrol trace particles), a light barrier (trigger) consisting of a 635-nm continuous wave laser with 1 mW power, and a pool. Figure 2 illustrates the experimental setup.

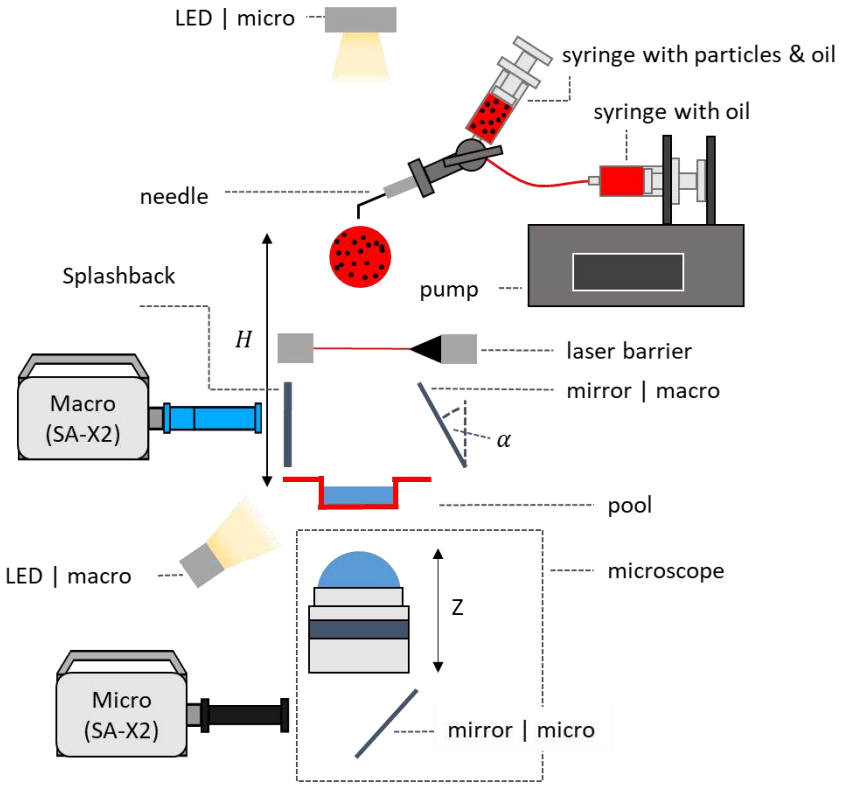


**Figure 2.** Schematic setup of the experimental facility for a given fall height $H$. It consists of the droplet generation system, the optical recording system and the impact area.

Defocusing is an optical principle that magnifies and blurs out-of-focus objects. This effect can be described using Newton's thin lens equation:

$$\frac{1}{f} = \frac{1}{S_O} + \frac{1}{S_i}. \tag{1}$$

where $f$ the focal length, $S_O$ the distance to the particle (object), and $S_i$ the distance to the image ray intersection point is. Figure 3 illustrates the defocusing effect schematically. To illustrate this, two particles are considered: a red particle located at the height of the focal plane and a green particle located above the focal plane. Particles that are in the focal plane are in focus, while particles that are not on this plane appear larger and blurred. The optical effect of variations in particle size and scattering pattern (intensity) is used to obtain three-dimensional information $(X, Y, Z)$ from a two-dimensional image $(X, Y)$ with the use of defocusing technique.

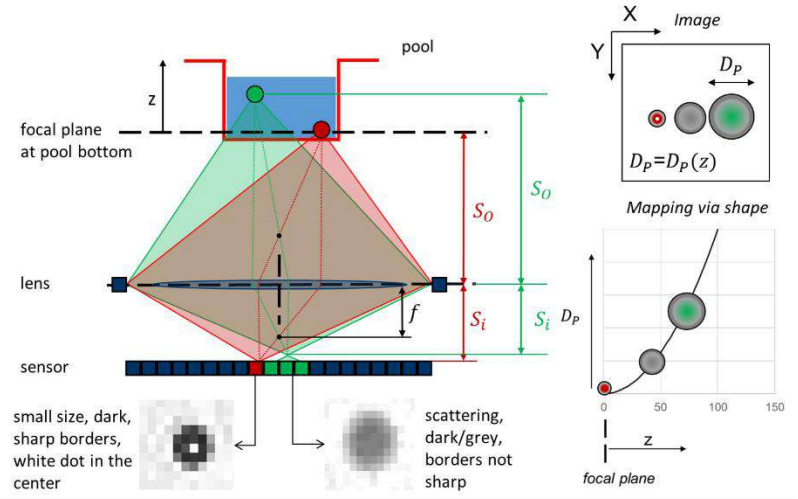


**Figure 3.** Schematic illustration of the optical principles of defocusing, with focal plane positioned at the pool bottom. This enables unique mapping of particles in 2D images $(X, Y)$ based on shape and scattering, providing 3D $(X, Y, Z)$ resolution. Additionally, having the focal plane at the pool bottom results in a reduction of the depth of field (DOF) by half. The green particles are located above the focal plane and occupy more sensors, while the red particles are in focus.

After the impact of the droplet in the pool, the formation of a crown crater is evident. By introducing particles into the droplet, the experimental µPTV setup enables the tracking of these particles in post-processing. The bottom view is used to determine the particle movement in the crown crater along $(X,Y)$, while the defocusing technique provides insights into motion along $Z$.

The primary method for determining the depth position of the particles involves comparing the experimental images in post-processing with a set of reference images, called calibration stack. Therefore, a particle with higher density than the pool fluid is introduced. The particle sinks to the pool bottom and remains in a stationary state. Subsequently, the microscope is adjusted to predefined positions, causing a shift in the focal plane. This results in the appearance of the blurry and enlarged effect. During this process, images are captured. Figure 4 shows in simplified form what this process looks like.

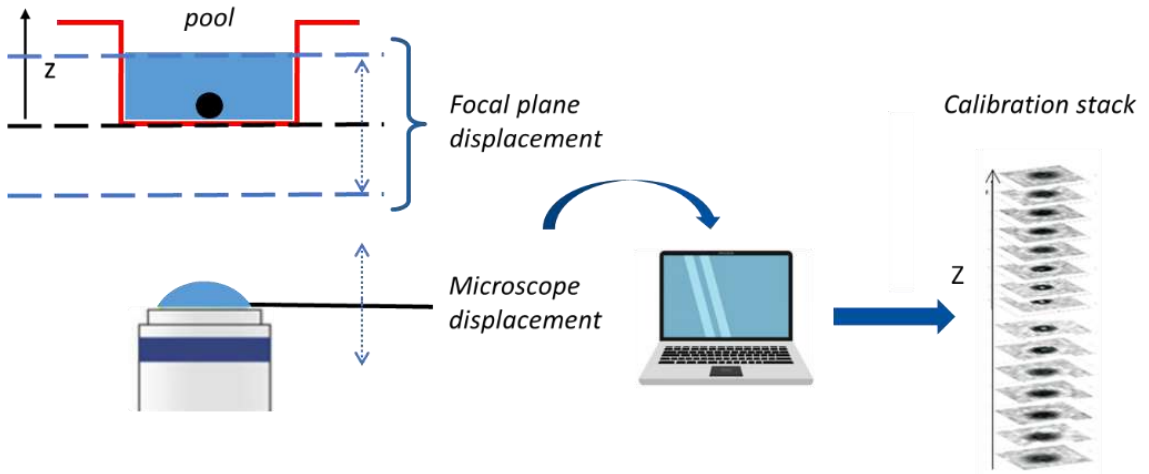


**Figure 4.** Creating a calibration stack - The microscope shifts its position to change the focal plane, resulting in blurry and enlarged particle images. At each predefined microscope step in z-axis, an image is captured.

The approach for investigating the 3D height evolution is divided into two sections. First, an calibration stack is created and then the 3D particle positions are reconstructed from the experimental images as part of the post-processing. In our measurement post-processing, we use the MATLAB code DefocusTracker based on the GDPT method. This method depends on the Normalized Cross-Correlation (NCC) algorithm, which relies on a user-defined Region of Interest (ROI). The primary aim of this approach is to assess the similarity between the ROI and the image with the correlation function $c(u,v)$: [3]

$$c(u,v) = \frac{\sum_{X,Y}[I_i(X,Y)-\bar{I}_i]\left[I_j(X-u,Y-v)-\bar{I}_j\right]}{\sqrt{\sum_{X,Y}[I_i(X,Y)-\bar{I}_i]^2 \sum_{X,Y}\left[I_j(X-u,Y-v)-\bar{I}_j\right]^2}}. \quad (2)$$

where $\bar{I}$ / $I$ the averaged / Intensity, $(u,v)$ the coordinates in the correlation space and $(X,Y)$ the coordinates in the picture is. The maximization of similarity occurs when $u = v$. The maximum peak value of the correlation function is stored as the similarity coefficient $c_m(i,j)$. The range of $c_m$ extends from 0 to 1, with 1 representing a perfect match, achieved when $i = j$, corresponding to the diagonal. A high-quality stack is characterized by significant differences in the generated images depending on $Z$, resulting in a variety of distinct $c_m$ values.

**Results and Discussion**

To create a calibration stack, the pool was filled with a thin layer of silicone oil (B20) and a few particles made of polystyrol. Due to sedimentation, particles $\rho_p = 1050\ \frac{\mathrm{kg}}{\mathrm{m}^3} > \rho_f = 955\ \frac{\mathrm{kg}}{\mathrm{m}^3}$ sink to the bottom of the pool. The thickness of the thin layer $h_{f,0}$ was measured using the Confocal Chromatic Imaging (CCI) method and amounted to $h_{f,0} = 0.37\ \mu\mathrm{m}$. As the microscope was moved along the Z-axis, the focal plane was adjusted, and a photo was taken at each step with 2 µm step size.

Figure 5 displays two shadow images of the pool bottom. In the first image, where the focal plane is very close to the pool bottom, we define $z = z_1$, and in the last image with $z = z_2 = z_1 + \Delta z$. The original image of 1024 x 1024 px² was cropped for clarity to approximately 130 x 190 px². For evaluation, the second particle from the top was selected at $(X,Y) = (71\ \mathrm{px}, 43\ \mathrm{px})$. Images 1' and 2' depict the particle for $z_1$ and $z_2$ within the region of interest (ROI). In green, the particle detection is performed in post-processing using our MATLAB code based on Rossi's and Barnkob's [1][2] GDPT method. The defocusing effect is recognized with a diameter increasing from 6 to 8 pixels.

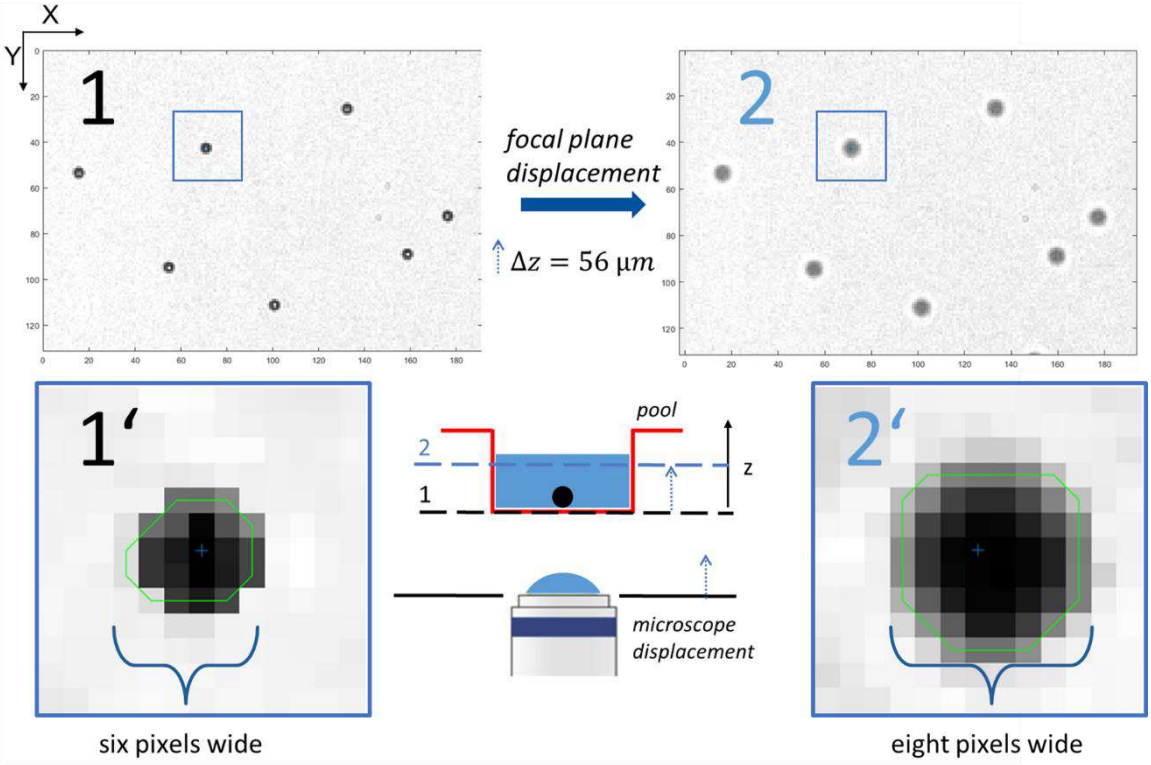


**Figure 5.** Pool bottom shadow images - Two shadow images of the pool bottom are presented. The first image, taken with the focal plane in close proximity to the pool bottom. The second image illustrates the defocusing effect at a microscope shift of $\Delta z = 56\ \mu m$. The particle size increases from 6 to 8 pixels.

In summary, the presented experimental setup allows for the generation of 2D data (X, Y) through the bottom view of the pool. The defocusing effect, leading to the blurring and enlargement of individual particles in the image, further enables the extraction of three-dimensional (3D) information (X, Y, Z). In the next step, we intend to investigate the impact of individual droplets on a thin liquid film from the bottom view. In this context, the GDPT method will also be applied. The information generated regarding the height (Z) of particles will then be matched with the calibration stack. Through this approach, we aim to gain insights into the 3D height evolution in the crown crater during early crown formation with the General Defocusing Particle Tracking (GDPT) method.

**Nomenclature**

| | |
|---|---|
| $D_0$ | Droplet diameter [m] |
| $U_0$ | Impact velocity of a single drop [m s^-1] |
| $\rho_{d,f}$ | Density of the trace particle ( $_d$) or droplet fluid and wall-film ( $_f$) [kg m^-3] |
| $\mu_{d,f}$ | Dynamic of the trace particle ( $_d$) or droplet fluid and wall-film ( $_f$) [kg m^-1 s^-1] |
| $\sigma_{d,f}$ | Surface tension of the trace particle ( $_d$) or droplet fluid and wall-film ( $_f$) [kg s^-2] |
| $h_{f,0}$ | Height of the wall-film [m] |
| X, Y, Z | Cartesian coordinates of a particle [m] |
| $C_x, C_x$ | Coordinate of the impact center [m] |
| $\bar{I}$ / $I$ | The averaged / Intensity [-] |
| $f, S_0, S_i$ | Focal point, distance to the particle (object), distance to the image crossing point [m] |

**References**

[1] M. Rossi, and R. Barnkob. A fast and robust algorithm for general defocusing particle tracking. Measurement Science and Technology. 32(1). (2021).
doi: https://dx.doi.org/10.1088/1361-6501/abad71
[2] R. Barnkob, and M. Rossi. DefocusTracker: A Modular Toolbox for Defocusing-based, Single-Camera, 3D Particle Tracking. Journal of Open Research Software. 9(1). (2021).
doi: http://doi.org/10.5334/jors.351
[3] Rune Barnkob and Massimiliano Rossi. General defocusing particle tracking: fundamentals and uncertainty assessment. Experiments in Fluids, 61(4), apr 2020. 7, 9, 18

# 360° Contact Angles of Water Droplets on Micrometric Ramps, Pyramids and Staggered Cuboid Surfaces at varying Wettability

P. Palmetshofer*[1], T. Arcos Marz[1], B. Weigand[1]
Institute of Aerospace Thermodynamics, University of Stuttgart, Germany
*Corresponding author: patrick.palmetshofer@itlr.uni-stuttgart.de

## Introduction

The apparent contact angle of a static droplet on a surface is often used to characterize the surface wettability. However, on regularly structured surfaces, this value can depend on the azimuthal angle of the measurement. We report the azimuthal variation of the apparent contact angle of a gently deposited sessile droplet on various regularly structured PMMA surfaces featuring stacked arrays of ramps in two sizes, pyramids and staggered cuboids. We also modify the surface wettability of the samples using plasma polymerization, thus applying a PTFE-like coating to the surfaces. We show how this results in both an increase of the apparent contact angle and in a reduction of its azimuthal variation.

## Material and methods

We used diffuse backlight imaging to measure the apparent contact angle of water droplets on Polymethylmethacrylate (PMMA) samples. The surfaces were manufactured using hot embossing after 3D direct laser writing. The investigated structures can be seen in figure 1. Details on the hot embossing process and a similar 2D laser writing process were previously described by Foltyn et al. [1].

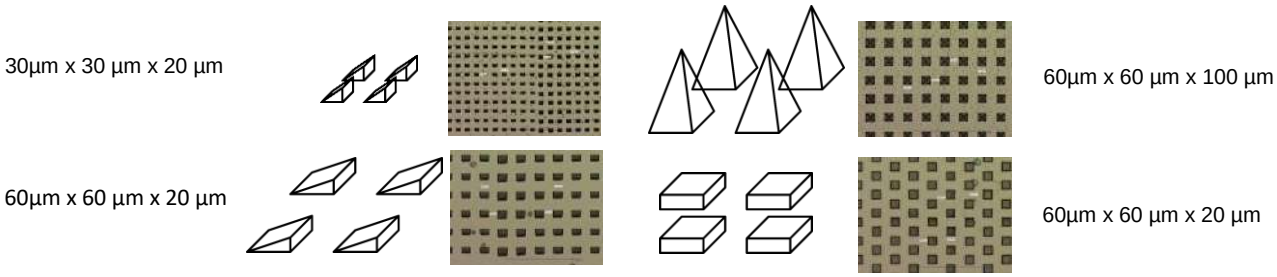


**Figure 1.** Surface structures

For the determination of the contact angles, we used the DataPhysics Optical Contour Analysis device modified by Foltyn [2]. In it, the dispensing tip and surface are contained in a chamber, which fixes the relative humidity to 98%. The windows in the optical path are heated to avoid condensation, which would interfere with the optical measurements. The samples are placed on a rotating platform to allow for the measurement of the contact angle from all sides. The droplets are set to 5 µL and are deposited onto the surface using a needle. Before rotating the surface the droplets are given 2 minutes to settle to their final position. The rotation stage is connected to the camera and a picture is taken in 1° increments. Figure 2 shows the experimental setup and details on the evaluation method can be found in the work of Foltyn et al. [3]. However, we used the DataPhysics software to analyze the contact angles.

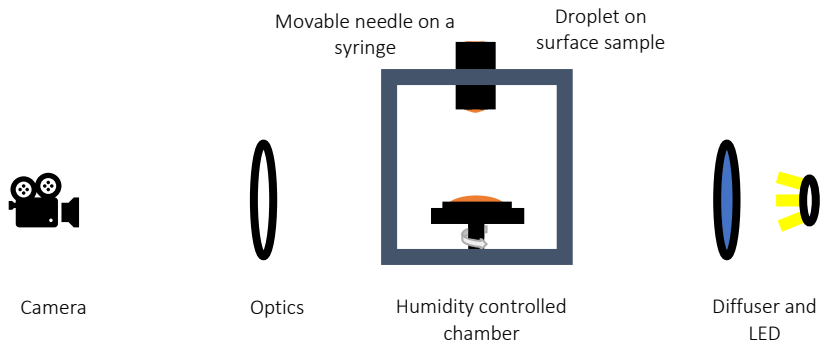


**Figure 2.** Experimental setup

The surface chemistry was modified by adding a nanometric PTFE-like layer through plasma polymerization. On flat untreated PMMA surfaces, the theoretical contact angle is 68°, while on a polymerized surface it is 120° [1].

**Results and Discussion**

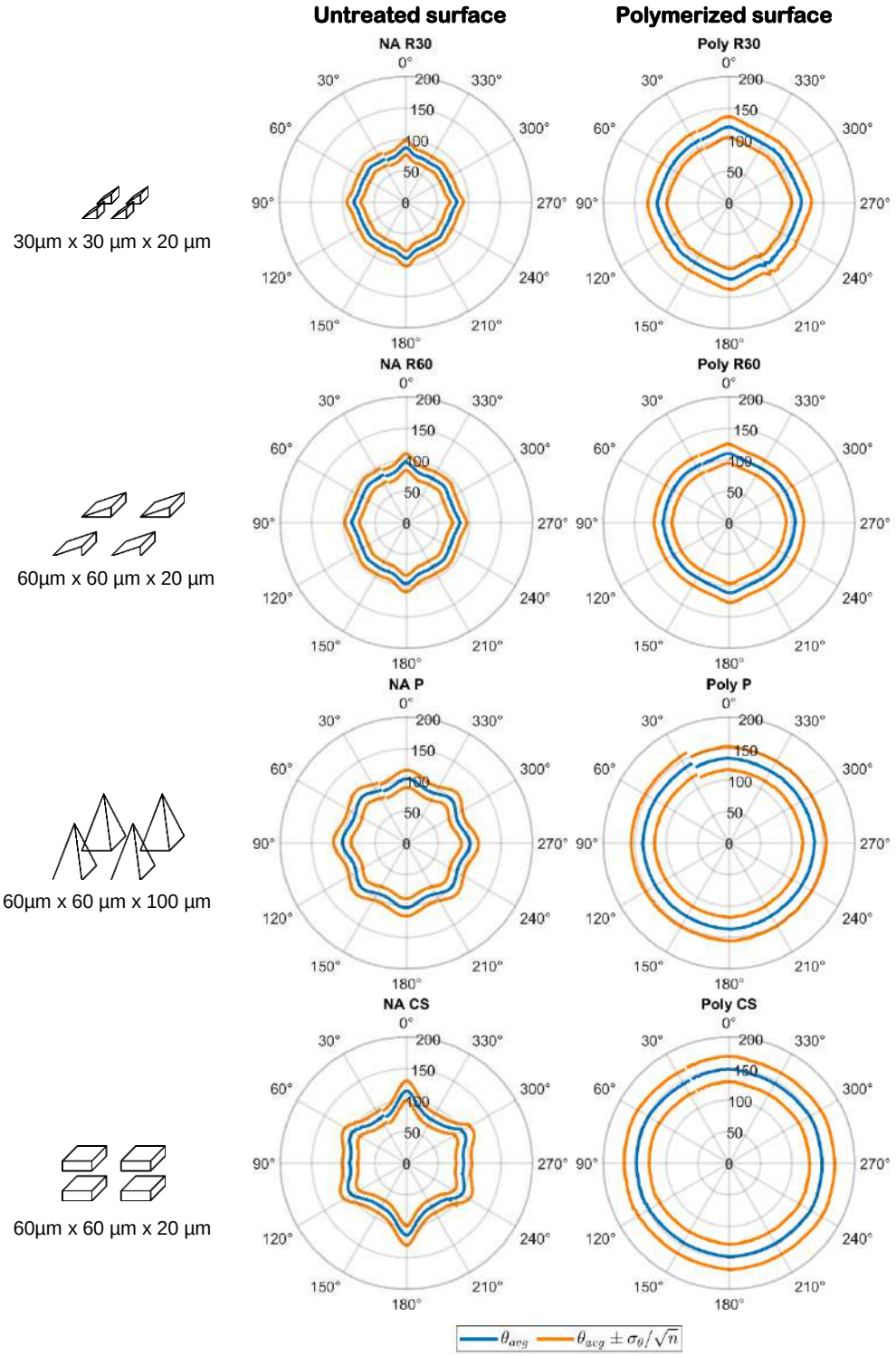


**Figure 3.** Selected results for the contact angle

Our results show how the variation of the apparent contact angle on non-cuboid and staggered cuboid structured surfaces over the azimuthal angle varies depending on the structure shape, size, arrangement and the surface chemistry. Figure 3 shows how for untreated surfaces the strongest dependence of the apparent contact angle on the azimuthal angle can be found for the staggered cuboids, whereas the strongest variation on polymerized surfaces is observed for the smaller structures. However, for all polymerized surfaces the effect of the azimuthal

angle is smaller than for the untreated cases. The pyramids feature an almost 4-axis symmetry, while the staggered cuboids only shows symmetry along one axis.
The apparent contact angle reported here corresponds to the average of the measured contact angle on the right and left sides. In the future, the determination of the contact angle will be performed for each side separately to account for the anisotropy of the ramp structures. Additionally, the samples will be used for droplet impact experiments and specifically investigated for the differences between these structures and the cuboid structures previously investigated by Foltyn [1].

**Acknowledgments**
This work was funded and supported by the German Research Foundation/Deutsche Forschungsgemeinschaft (DFG) in the scope of the International Research Training Group/Graduiertenkolleg "Droplet Interaction Technologies" (GRK 2160/2: DROPIT)

**References**
[1] Foltyn, P., Guttmann, M., Schneider, M., Fest-Santini, S., Wildenschild, D., and Weigand, B.: Fabrication and evaluation methods of microstructured surfaces for droplet impact experiments. Droplet Interactions and Spray Processes. Springer International Publishing, 2020, pp. 71–86.
[2] Foltyn, P., Droplet collisions with dry solid surfaces with variable wettability and topography. PhD thesis, 2022
[3] Foltyn, P., Restle, F., and Weigand, B.: 360 evaluation of projected contact angles of static droplets on structured surfaces. Droplet Impact Phenomena & Spray Investigations (DIPSI), Bergamo, Italy. 2019

# Numerical simulation of droplet impact onto structured surfaces

Rishav Saha* , Bernhard Weigand
Institute of Aerospace Thermodynamics, University of Stuttgart, Germany
*Corresponding author: rishav.saha@itlr.uni-stuttgart.de

## Introduction

The interaction of droplets with a solid surface has been a topic of great interest in the diverse area of science and technology such as aerospace, electronics, energy and materials. In recent years, a tremendous increased interest has developed on micro-structured surfaces. Most of these studies are carried out as experimental investigations. In contrast, there is still only a limited number of numerical works, which has been done to understand the fundamental physical mechanisms taking place for a drop impact on such surfaces. However, continuously increasing computer capabilities make it now possible to analyse drop impacts on textured surfaces in great detail by using Direct Numerical Simulations (DNS) for multi-phase flows. Thus, this project aims to numerically study in detail drop impact and wetting behaviour on textured surfaces and its effects when the surface is heated.

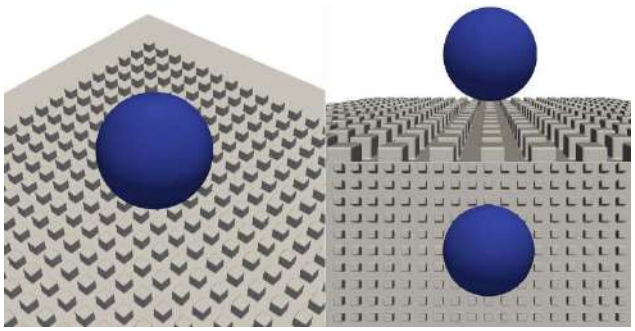

**Figure 1.** Numerical simulation of droplet impact on cubical micro-structured surfaces

## Methods

In this study, a computational fluid dynamics framework is employed to simulate the impact of an Iso-Propanol droplet onto a superhydrophilic cubical micro-structured surface under ambient conditions. The simulation tool used is the in-house DNS code Free Surface 3D (FS3D) [1]. The gas and the liquid phase are defined by Volume-of-Fluid (VOF) method, whereas the solid phase (cubical microstructures) is defined by Cut-cell method [2], which was implemented in FS3D. Reconstruction of the interface is done using PLIC [3]. Incompressible Navier-Stokes equation is solved using Finite Volume method.

## Simulation setup and assumptions

A spherical Iso-propanol droplet of 2mm impacts onto a cubical equally spaced non-heated micro-structured surface of sizes 500 µm (Case I) and 200 µm (Case II), at a velocity of 3.2 m/s and 1.7 m/s, respectively. The simulation is conducted to capture maximum spreading and splashing phenomenon. The droplet impacts exactly at the middle of a cubical pillars, therefore the spreading and splashing on the surface is considered to be symmetrical about the droplet impact direction. Hence, a quarter of the problem (one fourth of the droplet) is simulated to reduce the computational cost. The simulation domain size is 3.2Dx3.2Dx1.6D, where D represents the droplet diameter, with a resolution of 120 cartesian cells per droplet diameter, which is approximately 3.8 million cells in total. The simulations are conducted on AMD Ryzen 7 3700X 8-Core Processor.

**Table 1.** Simulation parameters for the two case with different pillar size, impact velocity and total simulation time.

| | Pillar size [µm] | Impact velocity [m/s] | Total simulation time [ms] |
|---|---|---|---|
| Case I | 500 | 3.2 | 1 |
| Case II | 200 | 1.7 | 4 |

## Results

The simulation result for the two mentioned cases show two different events, splashing and spreading. In figure 2 and figure 3, the splashing and spreading of a droplet impact at different time instances are shown, respectively.

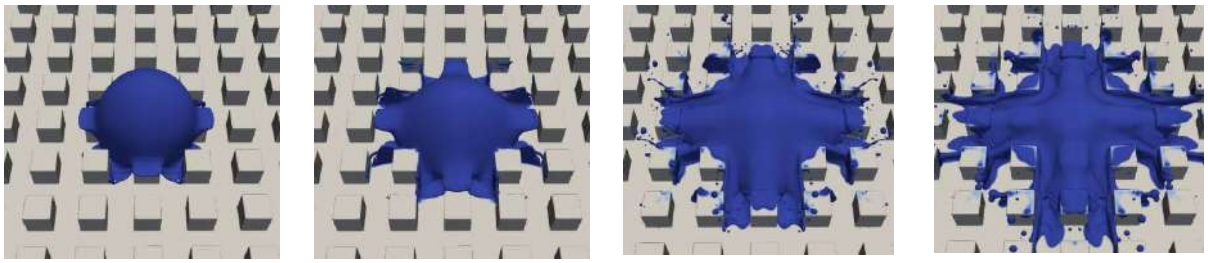

(a) $t$ = 0.3 ms (b) $t$ = 0.4 ms (c) $t$ = 0.6 ms (d) $t$ = 0.8 ms

**Figure 2.** Case I: Numerical simulation of 2 mm droplet impacts at a velocity of 3.2 m/s, onto a cubical micro-structured surface of size 500 µm, at different time instances $t$.

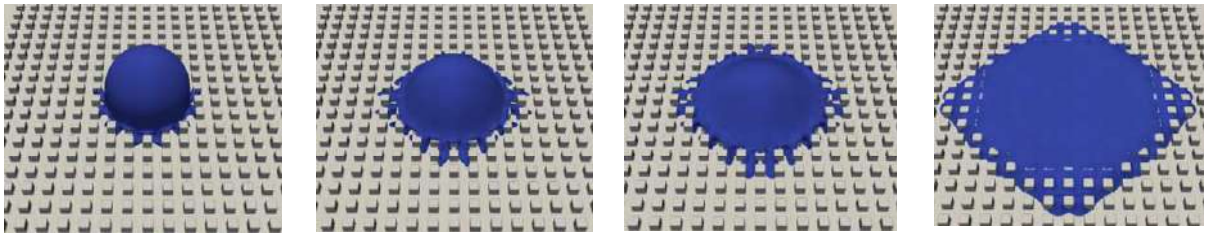

(a) $t$ = 0.4 ms (b) $t$ = 0.6 ms (c) $t$ = 0.8 ms (d) $t$ = 3.2 ms

**Figure 3.** Case I: Numerical simulation of 2 mm droplet impacts at a velocity of 1.7 m/s, onto a cubical micro-structured surface of size 500 µm, at different time instances $t$.

In figure 2, secondary droplet formation is seen, which is formed because of the high impact velocity. Here, the inertial forces are dominant, whereas in figure 3, the droplet hits at a lower weber number on smaller micro-structures, which creates a quadrilateral shape while spreading, an interesting area of the on-going research.

## References

[1] K.Eisenschmidt, M.Ertl, H.Gomaa, C.Kieffer−Roth, C.Meister, P.Rauschenberger, M.Reitzle, K.Schlottke and B.Weigand. Direct numerical simulations for multiphase flows: An overview of the multiphase code FS3D. Appl.Math. Comput.,272(2):508−517,2015.

[2] Baggio, Martina. Volume of Fluid Numerical Simulation of Drop Impact on Superhydrophobic Complex Solid Surfaces Embedded in a Staggered Cartesian Grid. Publisher Dr. hat, 2020.

[3] Rider, William J., and Douglas B. Kothe. "Reconstructing volume tracking." Journal of computational physics 141.2 (1998): 112-152.

# Experimental Observation of the Collision of a Crown with a thin Wall Film during Early Oblique Droplet Impact

J. L. Stober*[1], K. Schulte[1], M. Santini[2]
[1]Institute for Aerospace Thermodynamics, University of Stuttgart, Germany
[2]Department of Engineering and Applied Sciences, University of Bergamo, Italy
*Corresponding author: jonathan.stober@itlr.uni-stuttgart.de

**Introduction**

In most spray impact scenarios in technical applications, many droplets impact obliquely on a wetted wall. The mechanisms behind crown and finger formation as well as the splashing characteristic during oblique drop impact are not yet fully understood. Recent oblique impact experiments showed a sudden change in splashing characteristics with an increase in impact velocity. At a certain point, it changes from a late detachment of secondary droplets from one single central finger to splashing starting much earlier and many droplets detach from several fingers. Additional experiments with a higher magnification were conducted to make the early phase of crown development visible and to explain the change in impact morphology.

**Experimental Setup**

To achieve an oblique impact, the droplet has to be ejected with a horizontal velocity component. Figure 1 (A, B) shows the droplet generator, which was built for that purpose, based on the patent by Santini et al. [1]. It consists of a carriage which is accelerated back and forth in a controlled way by a linear motor. A blunt syringe needle is fixed on it and is supplied with Isopropanol by a piezoelectric pump. Figure 1 (C) illustrates the detachment process. During the high deceleration phase at the front turning point, the fluid within the needle is pushed outwards due to its own inertia and forms a ligament, from which droplets detach. Only the first droplet, with the highest velocity and diameter, reaches the impact point, while the subsequent droplets follow a shorter trajectory. In this study, a needle with an inner diameter of 1.5 mm resulted in droplets in the range of D ≈ 1.5 mm. The produced droplets are nearly spherically and do not oscillate as can be seen from Figure 1 (D), which shows the droplet prior to the impact on the film. Potential oscillations resulting from the forced detachment thus have been damped before impact.

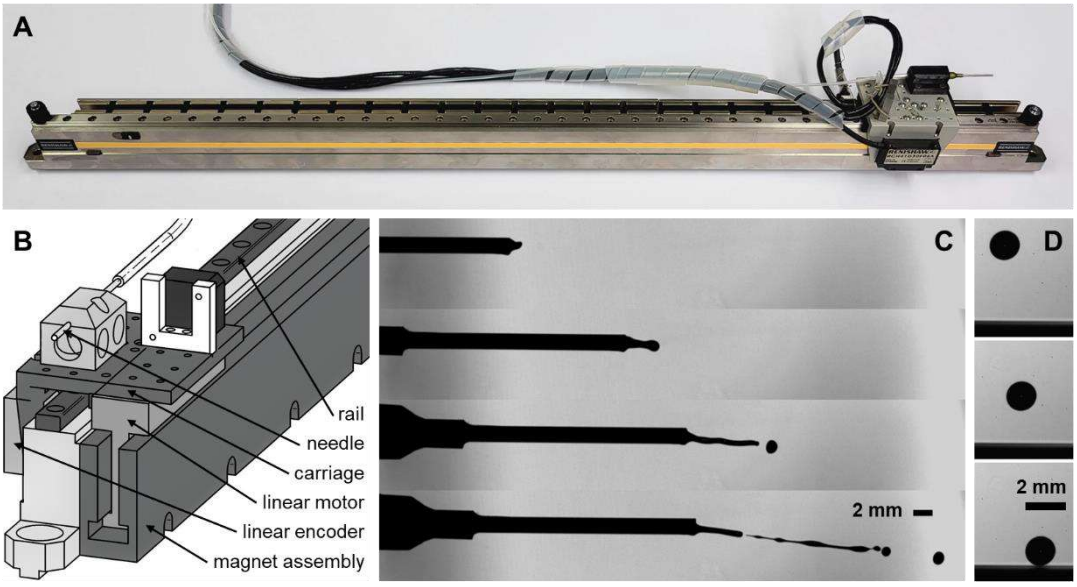


**Figure 1.** (A) Foto of the oblique droplet generator, (B) sketch of the droplet generator according to the patent by Santini et al. [1], (C) high-speed camera recording of the detachment process, (D) high-speed camera recording of droplet prior to impact onto the liquid film.

The experimental setup is illustrated in Figure 2. The imaging system comprises two synchronized high-speed cameras (Photron Fastcam SA-X2) capturing the process from two perspectives: a side view (blue dash-dotted line) and a front view (red dashed line). For each camera, an LED with a lens acts as a light source for the backlit shadowgraphy. The cameras record with a frame rate of 12,500 fps and a resolution of 1,024 x 1,024 pixels. This

results in a relative resolution of 12.1 µm/px for the side view and 21.1 µm/px for the front view. For the impact area, a smooth sapphire glass plate with a size of 50 mm x 50 mm and a thickness of 2 mm is used. The liquid film of isopropanol covers the complete glass plate and is held by its surface tension. The size of the glass plate ensures a flat film in the middle of the plate, where the droplet impacts. Its thickness is measured by a confocal chromatic sensor continuously from below during the experiment to monitor changes due to evaporation. The position and inclination of the droplet generator can be adjusted, as well as the detachment velocity. With that, different impact angles and velocities can be realized independently from each other.
A sketch of the oblique droplet impact onto a wall film is shown in Figure 3. The droplet diameter is determined utilizing an in-house Matlab program, which analyses the side view of the high-speed camera recordings, assuming a spherical shape. Similarly, the impact velocity and angle are also calculated using a Matlab program evaluating the last ten frames before impact. The three different impact conditions shown in this study are summarized in Table 1.

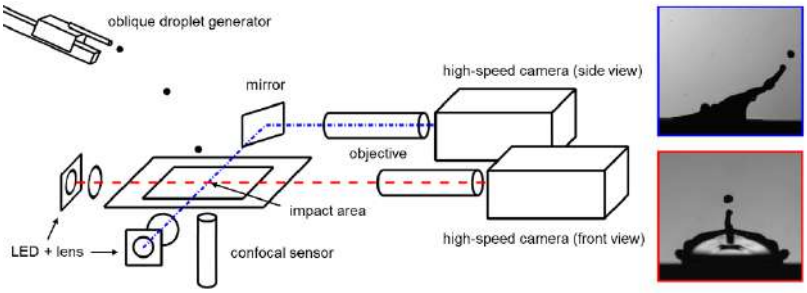


**Figure 2.** Schematic representation of the experimental setup.

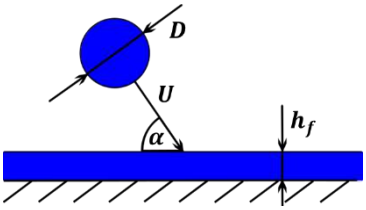


**Figure 3.** Sketch of an oblique droplet impact onto a wall film.

**Table 1.** Impact conditions and fluid properties at 22°C

| | Exp 1 | Exp 2 | Exp 3 | Uncertainty |
|---|---|---|---|---|
| Droplet diameter $D$ | 1.45 mm | 1.49 mm | 1.62 mm | ± 0.014 mm |
| Impact velocity $U$ | 3.10 m/s | 3.35 m/s | 3.38 m/s | ± 0.025 m/s |
| Impact angle $\alpha$ | 61.7° | 59.3° | 59.6° | ± 0.41° |
| Dimensionless film thickness $\delta$ | 0.26 | 0.24 | 0.22 | ± 0.004 |
| Weber number $We = \rho D U^2/\sigma$ | 508 | 610 | 675 | |
| Ohnesorge number $Oh = \mu/\sqrt{\rho\sigma D}$ | 0.143 | 0.141 | 0.136 | |
| Density ρ | 784.3 kg/m³ | | | |
| Surface tension $\sigma$ | 21.5 mN/m | | | |
| Dynamic viscosity $\mu$ | 2.24 mPa/s | | | |

**Results and Discussion**

Figure 4 presents high speed recordings of the experiments summarized in Table 1. In the left column, the side and front view of the crown development shortly after impact are shown, and in the right column, the resulting crown shape at maximum extension is shown for the front view. For experiment 1 there is no interaction of the early crown with the wall film (A1). This leads to an undisturbed growth of the crown with a stable rim. Only at the front one single central finger forms, from which secondary droplets detach consecutively (B1). With an increase in impact Weber number (experiment 2), the middle part of the early crown on the front side starts to touch the wall film (A2). This introduces disturbances to the rim at this part and leads to a partial rupture of the crown with the growth of two to four comparably thin fingers (B2). Multiple secondary droplets are ejected. With a further increase in Weber number the collision of the crown with the wall film intensifies. We now observe a collision of the complete front side of the crown and the ejection of tiny droplets (A3). This is followed by a rupture of the rim at the complete front half of the crown leading to many fingers and many secondary droplets (B3).
An increase in the number of fingers and secondary droplets with an increase in Weber number is well known and was described before for normal droplet impacts as well as oblique impacts, [2-3]. However, the here described change in splashing characteristic is not only resulting from the general increase in Weber number, but additionally by the collision of the early crown with the wall film. This leads to a more fundamental and sudden change in finger formation for small variations of Weber number.

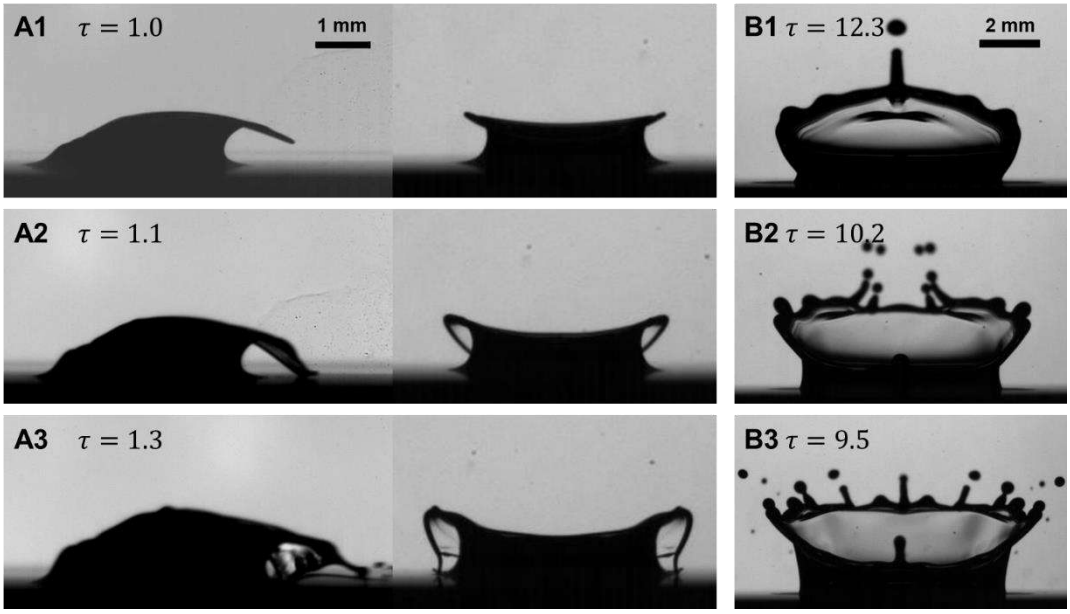


**Figure 4.** (A) Early crown morphology side and front view, (B) late crown morphology front view for Experiment 1 We = 508, Experiment 2 We = 610, Experiment 3 We = 675, at the dimensionless time after impact $\tau = tU/D$.

**Nomenclature**

| | |
|---|---|
| D | droplet diameter [mm] |
| $h_f$ | wall film thickness [mm] |
| Oh | Ohnesorge number [-] |
| U | impact velocity [m/s] |
| We | Weber number [-] |
| $\alpha$ | impact angle [°] |
| $\delta$ | dimensionless film thickness [-] |
| $\sigma$ | surface tension [mN/m] |
| $\mu$ | dynamic viscosity [mPa/s] |
| $\rho$ | density [kg/m³] |

**References**

[1] M. Santini, G.E. Cossali, M. Marengo, „Device and Method for Drops Generation“, WO 2010/021004 A1, PCT/IT2008/000554, 22 August 2008

[2] Cossali, G.E.; Coghe, A.; Marengo, M. “The impact of a single drop on a wetted solid surface.” Experiments in fluids 1997, 22, 463–472. https://doi.org/10.1007/s003480050073

[3] Okawa, T.; Shiraishi, T.; Mori, T. “Effect of impingement angle on the outcome of single water drop impact onto a plane water surface.” Experiments in Fluids 2008, 44, 331–339. https://doi.org/10.1007/s00348-007-0406-z

# The Use of Local Solutions to Model Phase Transitions in the Compressible Flow Regime

C.-D. Munz*, S. Jöns, P. Mossier, A. Travnicek, A. Beck
Institute of Aerodynamics and Gas Dynamics, University of Stuttgart, Germany
*Corresponding author: munz@iag.uni-stuttgart.de

**Introduction**

The idea in a sharp interface approach for two-phase interfaces is based on defining appropriate jump conditions to couple the bulk flows. Hence, local approximate relations are needed, which characterize the local thermodynamics at the interface. We use in the following the solution of the Riemann problem for two-phase flow with phase transition to obtain appropriate jump conditions and to establish the coupling of the macroscopic bulk phase simulations. Molecular interactions, governing the process of phase transition on a microscopic scale, are incorporated through evaporation models that promise a consistent entropy production. The validation of this sharp interface approach is done by comparing the results of a sharp interface macroscopic solution with molecular dynamics simulations. The simulations are based on the compressible flow equations. The viscous terms are neglected in these calculations and we consider the Euler-Fourier system. The heat flux is necessary to model the phase transition properly.

**Jump Conditions at the Phase Interface**

We restrict ourselves to consider an arbitrary fluid in a liquid and a vapor phase, i.e., a single-component fluid. The phase interface in the macroscopic description is assumed to be infinitesimally thin and to carry no mass nor energy. The phases may exchange mass, momentum and energy, which is based on the application of the conservation laws to the interface, as well as on the thermodynamic modelling. The jump conditions at the phase interface for mass, momentum and energy read as

$$[[\dot{m}]] = 0, \tag{1}$$

$$\dot{m}[[v]] + [[p]] = \Delta p_\Gamma, \tag{2}$$

$$\dot{m}[[e]] + [[vp]] + [[q]] = S^\Gamma \Delta p_\Gamma. \tag{3}$$

Here, $\dot{m} = \rho(v - S^\Gamma)$ is the evaporation mass flux per unit area, the double bracket $[[*]]$ denotes the jump across the interface, $\Delta p_\Gamma$ denotes the increase of pressure due to surface tension based on the Young-Laplace law,and $S^\Gamma$ denotes the velocity of the interface. In addition, the entropy balance has to be satisfied leading to the jump condition

$$\eta_\Gamma = \dot{m}[[s]] + [[\tfrac{q}{T}]] \geq 0, \tag{4}$$

where $\eta_\Gamma$ denotes the entropy production across the interface. Focus of the thermodynamic modelling lies on the fulfillment of the first and second laws of thermodynamics. The first law is covered by the energy jump condition (3). The second law corresponds to the entropy balance and the jump condition (4). To complete these macroscopic jump conditions, local information is needed in form of an evaporation model, e.g., to specify the entropy production term $\eta_\Gamma$.

**The Riemann Problem with a Phase Interface**

The Riemann problem is the initial value problem with constant data, which jump at one point. It describes locally the situation at an interface assuming a constant state at both sides of an interface. Its solution in time bears the information what happens locally at the interface in short. In bulk flow, it is a basic building block in finite volume schemes to calculate the fluxes between grid cells. It has an exact solution in the inviscid case, i.e. for the Euler equations. Here, we extent this solution of the Riemann problem in the bulk phases to the two-phase case with phase transition. In the following, we restrict ourselves to phase transition from one pure phase to another pure phase and call the phases liquid and gas. We will generally speak of evaporation. However, all considerations also apply to condensation.

We consider the two-phase Riemann Problem as the initial value problem with a constant liquid state on the left and a vapor state on the right. Similar to the classical Riemann Problem, waves emerge from the initial discontinuity to the right and left hand side – into the liquid and into the gas. In the two-phase Riemann problem, the phase interface occurs in the interior region together with the contact discontinuity, which move with the local fluid velocity. A diagram of the Riemann solution is shown in Figure 1. Here, a rarefaction wave travels into the liquid region, while a compression wave goes into the gas. The solution can be obtained iteratively, looking how both states can be connected by the corresponding waves satisfying the appropriate jump conditions. The detailed procedure is described in detail in [1]. We mention that we consider here an inviscid solution, which has a much simpler structure because of the constant states between the waves. However, the jump conditions at the phase interface include

the jump of the heat flux to catch the physical situation in a proper way. The effect of heat conduction is neglected for the waves running into the gas and the liquid to the left and right. Because for the coupling of the bulk simulations the states right and left of the phase interface are needed only and the bulk simulations contain the heat conduction terms this should be of minor importance.

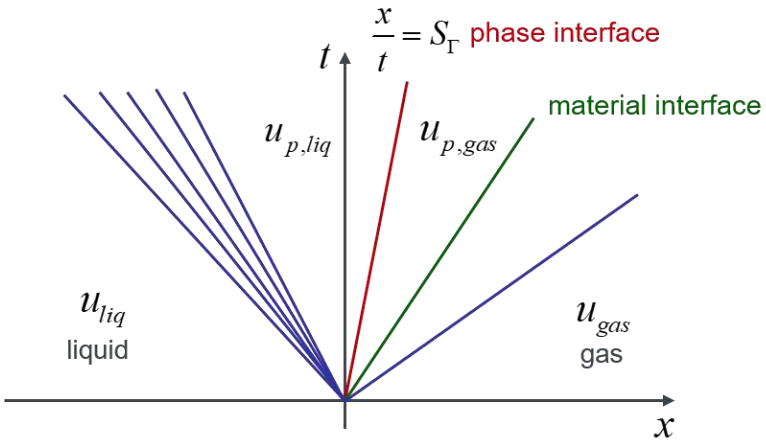


**Figure 1.** Diagram of the solution of the two-phase Riemann problem for a liquid and a gas interface with phase transition

**Numerical Results**

For validation, we compared the results of our numerical approach with results of molecular dynamic simulations. Our test problem is the two-phase evaporation shock tube, which was considered by Hitz et al. [2]. They studied the behavior of a saturated liquid that was put in contact with a superheated vapor with molecular dynamics simulations and a sharp-interface method. The vapor densities varied between 90%, 70% and 50% of the saturation density. To keep the interface sharp, we use a grid, moving with the velocity of the phase interface. The numerical method is a finite volume scheme of second order accuracy with a TVD limiter. The numerical fluxes are calculated by solving the classical Riemann problem in the bulk phases. The coupling was established by our two-phase Riemann solver. The evaporation model was based on Cipolla et al. [3]. We also considered an approximate solution of the two-phase Riemann problem. Figure 2 shows a comparison of all the results for 70% saturation density. The numerical results are in a very good agreement in density and velocity. Only directly at the shock wave, at about x = 700, the sharp-interface method predicts higher velocities than the molecular dynamics data. This aspect may be related to the absence of viscous terms in the mathematical fluid model while it is inherently contained in the molecular dynamic simulation. In temperature, the value of vapor is too high compared to the molecular dynamics data near the interface. The three Riemann solvers are in excellent agreement with each other, except for the vapor temperature near the interface. Here, both approximate Riemann solvers deviate from the exact solver and predict a slightly lower temperature. In combination with the ghost fluid method to keep the interfaces sharp, multidimensional simulations also show good results and high level of rubustness.

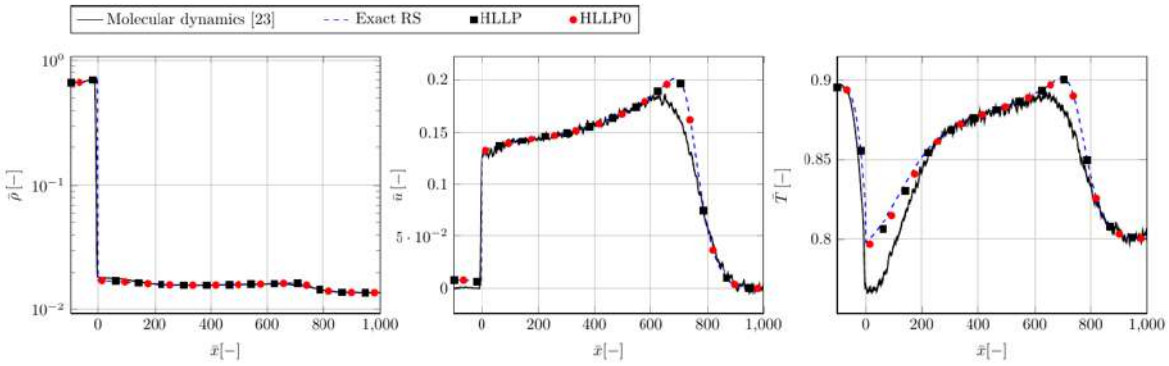


**Figure 1.** Diagram of the solution of the two-phase evaporation problem for a liquid and a gas interface with phase transition

**References**

[1] Jöns,S., Munz,C.-D., Applied Mathematics and Computation 440 (2023), 127624
[2] T. Hitz, T., Jöns, S., Heinen, M., Vrabec, J., Munz, C.-D., J. Comput. Phys. 429 (2021), 110027
[3] Cipolla, J.W., Lang, H., Loyalka, S.K., J. Chem. Phys. 61 (1974), 69–77

# Phase Change and Interaction Behaviour of Supercooled Water Droplets

V. Kunberger*[1], B. Weigand[1]
Institute of Aerospace Thermodynamics, University of Stuttgart, Germany
*Corresponding author: verena.kunberger@itlr.uni-stuttgart.de

## Introduction

The phase change and interaction behaviour of supercooled water droplets is of great importance to understand the processes in clouds and precipitation. These micro-processes are relevant for the development and improvement of climate models and weather forecasts [1].
The ambient conditions in clouds are extreme with temperatures as low as -40° C and lead to the supercooling of water droplets. The following phase change and freezing of the droplets is one of main energy sources in clouds or more severe weather phenomena like cyclones [2] as latent heat is released during that process. This also influences the clouds on a macroscopic scale as droplets in the vicinity of the latent heat release evaporate and therefore the cloud size is limited [1].
Phase change is initiated by either homogeneous nucleation or by heterogeneous nucleation through particles like aerosols or ice crystals. Supercooled droplets are in a metastable state of the Gibbs Free Energy

$$G = U - TS + PV \tag{1}$$

and for them to change into the stable solid phase, they have to overcome the energy barrier

$$\Delta G^* = \frac{16\,\pi\sigma^3}{3\,\Delta G_V^2} \tag{2}$$

This is a statistical process and the probability overcoming the energy barrier is dependent on the degree of supercooling [3].

Due to convection, the supercooled water droplets are in constant motion in the clouds and interact and collide with each other. Thus, the question arises if the droplets themselves can trigger nucleation by colliding with each other. This is possible if the energy of the impact is large enough to overcome the energy barrier mentioned in equation (2) and therefore depends on the impact velocity and droplet size and the degree of supercooling. But also the ambient conditions need to be taken into account as the surrounding gas has to transport the latent heat released during the freezing process away which is dependent on the conduction and convection properties of the ambience. This means that the rate of freezing is dependent on the surrounding gas and its heat transfer ability.

Furthermore, the interactions of several droplets are of interest as this is the onset of precipitation. As the supercooled water droplets move through the clouds, they can collide with snowflakes and freeze onto them. This is called riming and snowflakes fully covered in rime are called graupel [4]. If the impact energy of the droplets is higher due to higher velocity in more severe weather conditions, clear ice and a denser structure is formed which can result in hail [1,5].

The experimental methods to research these micro-processes and the main influences of temperature and relative humidity on them will be explained briefly in the next section as well as some results will be shown.

## Experimental methods

To research the binary collisions of supercooled water droplets with minimal disturbances, an optical levitation setup is used in which the laser holds the droplet in a stable position in a cooling chamber. Laser levitation is described in more detail by Ashkin [6]. The wavelength of the laser is chosen such that it is not absorbed by the water. The experimental setup is shown in Figure 1.

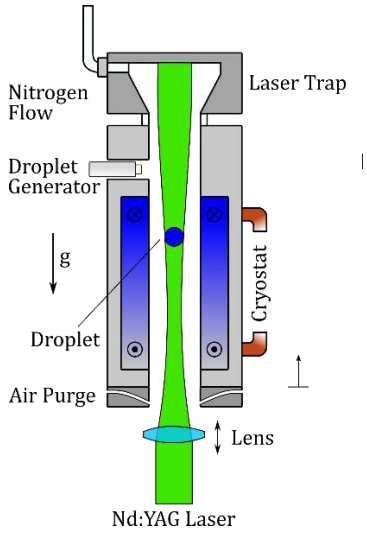


**Figure 1.** Experimental setup of the levitation of a supercooled water droplet

The droplets are produced by a droplet generator driven by a piezo-electric dispenser from microdrop Technologies and they have a size of 45 µm.
The chamber can be cooled down to -40°C and the relative humidity is controlled by a constant nitrogen flow within the chamber.
Through PMMA windows, optical access for backlight-imaging is given which is realised with a LED and a 12MP CCD camera. To detect the freezing point of the droplets, two PSD sensors record the scattered light of the laser and the change of polarisation which is caused by the freezing of the droplet.

As the laser beam is not strong enough to hold more than two small droplets, another setup is needed to look at the interactions of several supercooled water droplets. It looks similar to the levitation setup and is shown in Figure 2. This setup also consists of a cooling chamber, droplet generator and nitrogen supply, but a small aluminium surface is inserted on which the droplets impact. The surface is cooled down to ambient temperatures which is controlled by thermocouples in the surface. The droplet generator is moved randomly across the surface by two linear motors to simulate the random motions in clouds. The structures the form are observed with backlight imaging, a zoom-lens and a 12MP CCD camera. The droplet generator produces single droplets or groups of droplets on demand with a size of 75 µm.

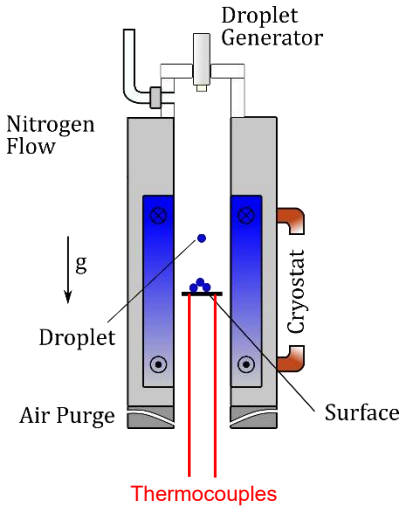


**Figure 2.** Experimental setup of interactions of several supercooled water droplets on a surface

**Results and Discussion**

Experiments were conducted at -37.5 °C and a relative humidity of 30% the first collisions observed are shown in Figure 3 below.

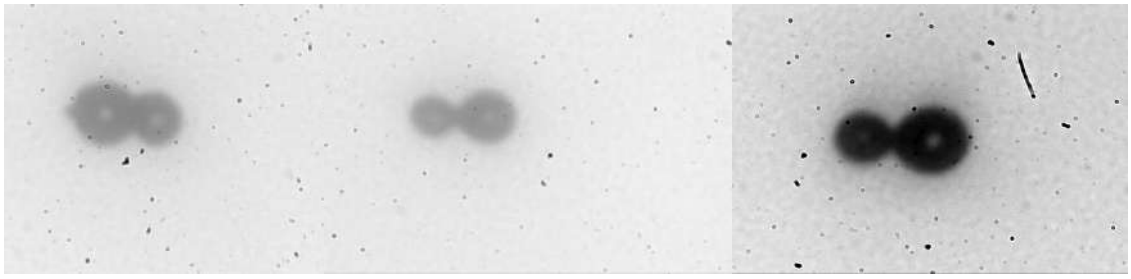

**Figure 3.** Binary droplet collisions of supercooled water droplets at 37.5°C

The smaller of the droplets is the one which is levitated first and subsequently evaporates and sublimates before the larger droplet collides.

It can be seen that the droplets freeze immediately on impact and remain mostly spherical. Therefore, the freezing process is very fast and the latent heat is transported away quickly. A spike in the larger droplet in the first image is also clearly visible which indicates a frozen droplet.

The sublimation process can also be observed in the collision product and the reduction of its size over time as shown in Figure 4.

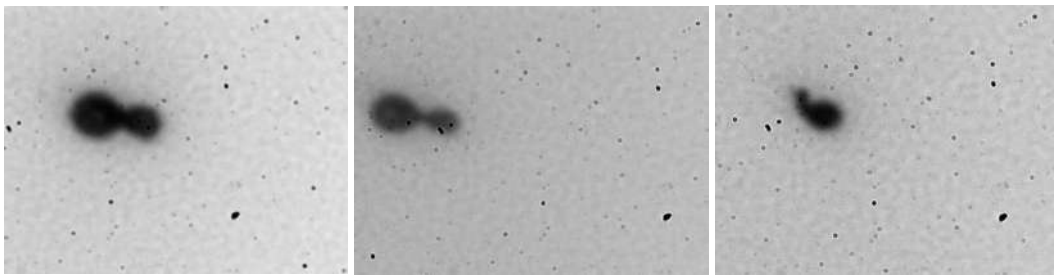

**Figure 4.** Sublimation of collided and frozen supercooled water droplets at 37.5°C

Future work will extend these experiments to different temperatures and also study the influence of relative humidity on the outcome of the collisions of supercooled water droplets.

In the setup to research interactions of several droplets on a surface, preliminary results were obtained. At different temperatures, structures of different densities were observed.

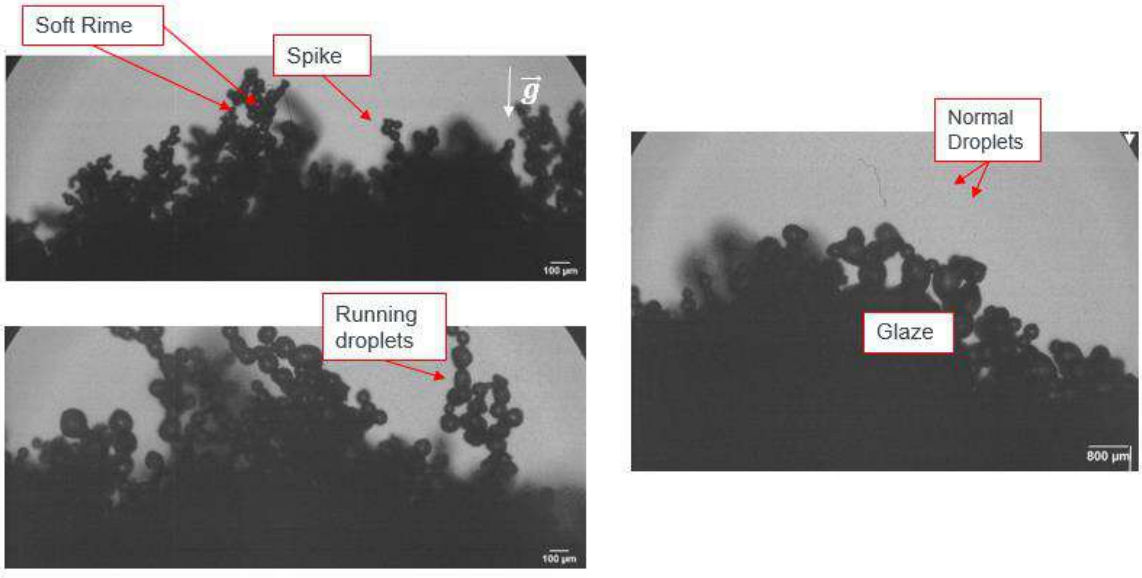


**Figure 5.** Freezing timescales of supercooled water droplets in different conditions

The images in Figure 5 show these structures that form if several droplets interact with each other. Depending on the conditions, they can form soft rime with larger gaps in between resulting in a loftier structure. But also denser structures and 'running droplets' that do not freeze instantly freeze could be observed for higher relative humidities. In very humid conditions, glaze ice that is very dense could be seen and larger deformed droplets.
But as these results are very preliminary, extended studies have to be performed in the future to relate the formation of different types of ice and rime to the conditions found in the chamber.

**Nomenclature**

| | |
|---|---|
| G | Gibbs Free energy [J] |
| U | Internal Energy [J] |
| T | Temperature [K] |
| S | Entropy [J $K^{-1}$] |
| P | Pressure [Pa] |
| V | Volume [$m^3$] |
| σ | Surface Tension [N $m^{-1}$] |
| $\Delta G_V$ | Latent Heat [J] |

**References**

[1] Pruppacher, H. R., Klett, J. D., 1997, 'Microphysics of clouds and precipitation'. Kluwer Academic Publishers.
[2] A. Khain, M. Ovtchinnikov, M. Pinsky, A. Pokrovsky, H. Krugliak, 2000, Atmospheric Research, 55(3), pp. 159-224.
[3] Kelton, K.F. and Greer, A.L., 2010, 'Nucleation in condensed matter – Applications in Materials and Biology', Elsevier
[4] A. Rango, J. Foster, E.G. Josberger, E. F. Erbe, C. Pooley, W. P. Wergin, 2003, SCANNING, 25, pp. 121–131.
[5] W.C. Macklin, 1962, Q.J.R. Meteorol. Soc., 88, pp. 30-50.
[6] A. Ashkin, 2000, IEEE Journal on Selected Topics in Quantum Electronics, 6 (6), pp. 841-856.

# Author index

**Progetto grafico:**
**Servizi Editoriali – Università degli Studi di Bergamo**
**Università degli Studi di Bergamo**
**via Salvecchio, 19**
**24129 Bergamo**
**Cod. Fiscale 80004350163**
**P. IVA 0161280016**